Spring 2013

Strain Measurement Validation Using 3D Photogrammetry Techniques

Tori Chinn
San Jose State University

STRAIN MEASUREMENT VALIDATION USING 3D PHOTOGRAMMETRY TECHNIQUES

A Thesis

Presented to

The Faculty of the Department of Mechanical and Aerospace Engineering

San José State University

In Partial Fulfillment

of the Requirements for the Degree

Master of Science

by

Tori Chinn

May 2013

The Designated Thesis Committee Approves the Thesis Titled

STRAIN MEASUREMENT VALIDATION USING 3D PHOTOGRAMMETRY TECHNIQUES

by

Tori Chinn

APPROVED FOR THE DEPARTMENT OF

MECHANICAL AND AEROSPACE ENGINEERING

SAN JOSÉ STATE UNIVERSITY

May 2013

Dr. Fred Barez	Department of Mechanical Engineering
Dr. Eduardo Chan	Department of Mechanical Engineering
Mr. Michael Ospring	NASA Ames Research Center

ABSTRACT

STRAIN MEASUREMENT VALIDATION USING 3D PHOTOGRAMMETRY TECHNIQUES

By Tori Chinn

This project was conducted to validate the measurement of static strain and dynamic frequency in an aluminum beam using 3D photogrammetry technology against analytic modeling and conventional strain measurements. A review of the 3D photogrammetry literature was conducted and a summary is presented here. Static load displacement and strain were compared between analytical calculations, photogrammetric data, strain gauges, experimental measurements, and an FEA model. First mode forced vibration was validated between analytical work, FEA, accelerometers, and photogrammetric measures. Results yielded positive and repeatable correlations between photogrammetric data and analytical computations with most reliable results for displacement.

ACKNOWLEDGEMENTS

This project is the result of the efforts of many individuals. Much appreciation to the faculty and staff in the SJSU Mechanical Engineering Department with special thanks to Dr. Barez and Dr. Chan. Many thanks to the staff at NASA Ames for the mentorship from many talented and amazing engineers. Special thanks to Mr. Michael Ospring, Dr. Alberto Makino, Ms. XinXin Nee, and Mr. Frank Pichay for their time and support for this project. Finally my thanks to my family and friends. Without the belief, patience and support of all these people, this master's thesis would never even have been started.

TABLE OF CONTENTS

NOMENCLATURE

DIC	Digital Image Correlation
ESPI	Electronic Speckle Pattern Interferometry
FEA	Finite Element Analysis
HMI	Human Machine Interface
NVH	Noise, Vibration, and Harshness testing
PIV	Particle image velocimetry
USCU	United States Customary Units

LIST OF TABLES

LIST OF FIGURES

1.0 INTRODUCTION

1.1 MOTIVATION

NASA must test materials for performance during operational conditions, such as high stress conditions. One newer technique for stress testing is photogrammetry. An important area for improved stress testing is evaluating stress on wind tunnel compressor blades. Such testing also provides a way to begin evaluating this new technique.

Wind tunnels are used widely in the aerospace industry to experimentally validate analytical models. Tests conducted in these wind tunnels save money by ensuring prototypes behave as predicted before designs are put into full production. The air flow in a wind tunnel is driven by axial air compressors. The blades in an air compressor travel at high velocity and are exposed to high thermal loads that increase the stress and strain experienced by the blades. The blades in NASA Ames Unitary Plan Wind Tunnel 11x11 compressor rotate at a maximum operating speed of 645 rpm (3870 deg/s) with a blade tip velocity of 555345 in/s. Failure of air compressor blades poses a critical risk to the safe and efficient operation of a wind tunnel. Because of this risk it is important to fully understanding the stress and strains in the air compressor blades. The goal of this research is to validate strain measurement technology that provides a fuller strain profile at lower costs, thus increasing safety.

The eventual goal is to validate 3D photogrammetry technique as a method for measuring strain on the Unitary Plan Wind Tunnel 11x11 compressor blades, shown in

Figure 1. It was decided that a simple cantilevered beam would be a preliminary step before testing the compressor blades. The simpler geometry allows for the use of closed form solutions from classical beam theory as an analytical check.

This paper describes a survey of the existing literature on photogrammetry, historical testing of the compressor blades, and the research conducted on the cantilevered beam.

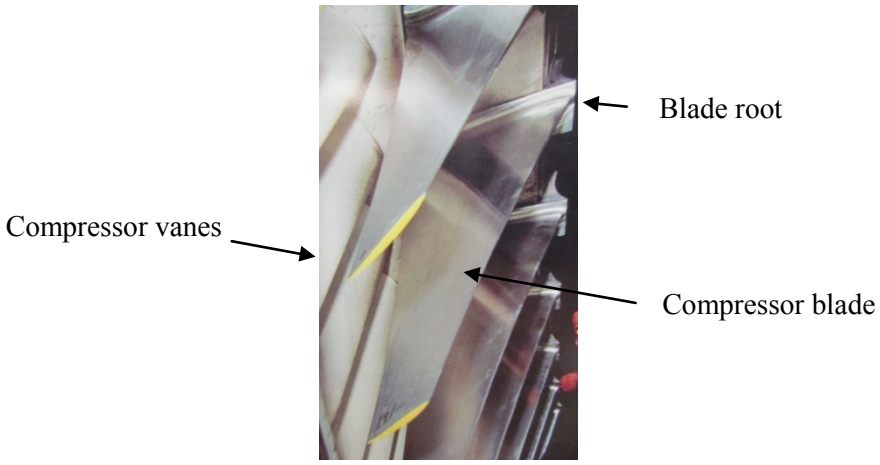

Figure 1 - Unitary Plan Wind Tunnel Compressor Blade

These compressor blades have been well characterized using traditional strain gauges. Nguyen, Guist, and Muzzio [1] performed an experimental investigation in 1992 that characterized the rotor blade vibration problem in the 11-by 11-foot Transonic Wind Tunnel at NASA Ames Research Center. In 1991, strain gauges

identified a resonance at certain frequencies that produced a much higher dynamic stress than was previously thought to exist in the wind tunnel blades. These stresses exceeded the bending cyclic fatigue limit of 10 ksi for the aluminum alloy 2014-T6 blades, and operation of the wind tunnel was restricted to reduced tunnel total pressure while moving through the resonant frequency band. Two types of frequency mistuning issues were identified. In the first type, the rotor disk and blades vibrated as a system that produced highly variable blade responses. Rotor blades responded more intensely at the lower frequency spectrum than blades at higher frequency. The second type of mistuning involved a coupling among rotor blades through the compliance of the rotor disk. A modal analysis of the bladed disk assembly was conducted and the frequency response, mode shape, and modal damping values of the system were obtained. Dynamic stresses of the compressor were measured using traditional strain gauges at RPMs ranging from 300-700 RPMs. Characterizations of modal frequency and resonance profiles of the rotor disk and rotor blade were used to implement two solutions to the vibration problem. An intended permanent solution was to fabricate composite blades that had increased material damping properties as compared to the existing aluminum blades. The temporary solution, using viscoelastic tape at the root block as an external damping mechanism, was proven as a viable solution for the aluminum blades until the composite blades were installed.

Polyurethane viscoelastic damping tape was tested in a more in depth investigation on the 11x11-foot Transonic Wind Tunnel for additional damping and

vibration suppression on axial flow compressor rotor blades [2]. The compressor blades are permanently attached to dovetail-shaped root-blocks that slide into a matching dovetail root geometry that serves as the retention area of the compressor rotor. Damping tape provided a damping increase of rotor blade bending modes by a factor of 6-10. There was an increase in damping in torsional modes by a factor of 2. The damping occurs from the shearing action at the dovetail interface plane on a thin layer of polyurethane adhesive tape attached to the dovetail. The implementation of the dovetail damping tape significantly reduced the compressor rotor blade vibration. The large reduction in all resonant stresses in the compressor allowed for more efficient operation of the 11x11-ft transonic wind tunnel. These tests used the state of the art technology of the time. Newer technology has the potential to provide a deeper understanding of stress and strain in the compressor blades.

1.2 STATE OF THE ART AND LITERATURE REVIEW

The use of strain gauges in the examination of strain for the wind tunnel compressor blades is a well-trusted technique. However, strain gauges must be carefully applied individually. Each strain gauge must be wired and attached to a data collection unit. Strain gauges must not be placed in areas that display high stress gradients because the results can be misleading, indicating a strain that is much higher than is experienced by the rest of part. In addition, strain gauges report only an average

strain in the area to which the strain gauge is attached. In an area of a high stress gradient, the gauge can give reading significantly lower than peak strain.

An alternative method of collecting strain measurements is photogrammetry. Photogrammetry is a technique in which the location of points in 3D space can be determined through geometric analysis of a pair of 2D photographic images taken a known distance apart with a known camera angle as seen in Figure 2. The points in space can be mathematically related to one another to create a 3D model of the object from the 2D images [3].

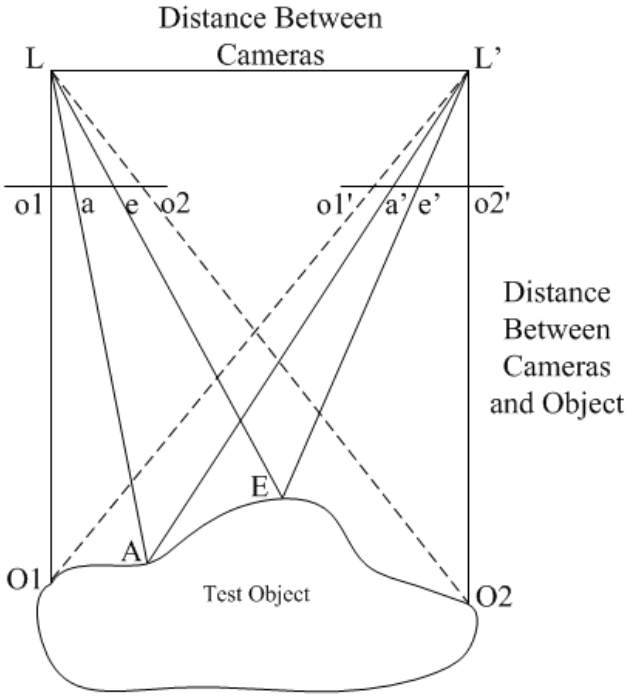

Figure 2 - Photogrammetry Principle

If load is applied between the capture of initial and subsequent 3D models, the difference in location between the same points in the initial and subsequent 3D models is the displacement, which can be used to determine the strain caused by the load. Using this 3D photogrammetry technique, strain can be determined. Once strain is determined either with strain gauges or photogrammetry techniques, stress can be calculated from strain by hand or with a computer script. Traditionally, this has been a manual process using relatively few points, and the calculations were painstakingly made graphically and analytically [4]. With the application of digital photography and modern computing technology, a full field of points can be tracked and the data more quickly analyzed. Digital photogrammetry is less labor intensive than using strain gauges, and provides a full field of strain data rather than the single point measurements provided by strain gauges. The photogrammetry technique to measure stress does not require the application of strain gauges and this provides many advantages and offers potential advancements in the field of engineering.

Photogrammetry is also known in the field as "full field strain measurements" and "3D image correlation" [5]. Photogrammetry determines strain and displacement by correlating points of a pattern on the test object in each camera image using geometric principles. The random or regular pattern was applied directly on a test object, generally with paint. Those markings, or correlational areas, are known as micro-image facets, and the center can be thought of as an extensometer and strain

rosette. Through photogrammetry, 3D coordinates of the visible surface were calculated. Rigid body motion does not have an effect on the measurements.

One advantage of photogrammetry over single point strain gauges is that data produce 3D full field visualized strain gradients in homogeneous, non-homogeneous, and anisotropic materials. This allows for the visualization of unpredicted high strain areas. Another benefit of full field strain results is that they can be directly compared to finite element analysis results, which can reduce time to deployment and potentially decrease the number of prototypes needed. Measurements previously impossible are now possible to collect using photogrammetry techniques.

Photogrammetry has been used to test high-temperature full field measurements. Strain data was collected on materials that were previously hard to test such as thin films, tissues, and artificial muscles. This technique could also be used to collect dynamic deformation measurements on such things as ballistic impacts, high-speed fracture mechanics, high-speed tire dynamometer testing, and ultra-high-speed spin-pit testing.

The 3D Electronic Speckle Pattern Interferometry (ESPI) technique is another visual strain measurement technique. In ESPI, the sensor also projects a speckle pattern of coherent light onto the test part and tracks the lateral movements of the speckles. The fringes indicate displacement isolines. In comparison to ESPI, 3D image correlation uses two cameras to correlate speckle patterns applied directly to the test piece, which is illuminated with ordinary white light. Electronic Speckle Pattern

Interferometry is very accurate, ranging from 0.03 to 0.35 microns, whereas 3D image correlation photogrammetry is 1/30,000 field of view, which is 0.3 to 30 microns [5]. However, a drawback of the ESPI technique is that because the speckle pattern is projected onto the test piece, the test setup is sensitive to ambient vibrations. Once the speckle has shifted the distance of its own diameter, the measurement can no longer be taken. Displacements in the X, Y, and Z directions cannot be taken simultaneously due to different illumination set ups required for in-plane and out-of-plane displacements, which limit dynamic measurement capability. Because 3D image correlation uses photogrammetry on an applied speckle pattern, it has a larger dynamic range. 3D image correlation measurements can be taken simultaneously in the X, Y, and Z axes.

An example of the use of 3D image correlation photogrammetry technique on non-homogeneous material was testing on ionic polymeric material [5]. This material can undergo large dynamic deformations and is used in robotics, artificial muscles, and dynamic sensors. Decreased shutter time prevents blurred images so intense illumination was used. The cyclic fatigue test setup had cameras synchronized to trigger at displacement peaks. Results included full-field strain values and quantitative results extracted from a sectional line. A full animation of strains was shown on the deforming 3D shape.

Photogrammetry can be used for testing in the super dynamic range and an example of this type of test was performed on the high-speed fracture of a rubber sample [7]. The notched rubber dog bone specimen was prepared with a stochastic

speckle pattern. High intensity halogen lights were used to reduce camera exposure time to a fraction of a millisecond, which reduces blurring. Frame rates can be significantly increased from 1000 frames per second at full 1024 x1024 resolution to 7400 frames per seconds at 512 x 512 pixel resolution.

Photogrammetry can also be used in the super dynamic range to get data from road tire dynamometer testing. For this type of testing, the shortest shutter speed may not be able to prevent blurring of the applied pattern during camera exposure. In cases like this, 500 nanoseconds of pulsed arc discharge light were used [7]. For this setup, the arc lamp pulsed light was appropriate for testing of automotive tires up to speeds of 150 mph. The pulse was generated with a slip ring encoder on the tire. The slip ring encoder generated an index pulse once per rotation that triggered a pulse/delay generator. Time delay was varied to synchronize the tire rotational position to the pulsed illumination.

Photogrammetry can be used in super dynamic range tests for spin pit testing, which is used to test for centrifugal strength, verify stress analysis, and establish fatigue life. A composite fly wheel with a flat surface was used as the test subject. Because out-of-plane motion would cause errors in the strains due to magnification changes in the applied pattern, only one camera was used and in-plane strains were measured using 2D image correlation. A thick polycarbonate viewing window was used to protect the camera in case the flywheel burst. A pulsed YAG laser was used to reduce the exposure time for each image to six nanoseconds. Image capture was triggered by a

once-per-revolution signal from the tachometer, which provided input to the precision trigger module. The module then opened the camera shutter within 5 microseconds [7]. Synchronized signals from the camera shutter were delayed before being output to trigger the pulsed laser. This delay controlled when the laser pulse would illuminate a targeted rotational position. It was found that centrifugal strain at inner and outer locations at 7 different RPMs speeds were essentially the same. However, radial strain on the inner locations was approximately three times higher than that of the outer locations at different RPMs. Key modifications that allow for un-blurred image capture at high speeds are the decrease in shutter exposure time as well as synchronized flash illumination of coherent or non-coherent light, depending on the application.

Photogrammetry is versatile in its ability to scale to the very large or very small sized projects. Paulsen, Erne, Moeller, Sanaw and Schmidt [8] performed a study detailing the use of videogrammetry (photogrammetry using video) on a large wind turbine during operation. Benefits of this type of testing allows for the entire complex structure to be tested dynamically instead of piecewise testing.

Tyson, Psilopoulos, Schwarts and Galanulis [9] summarized the application of 3D digital image correlation (DIC) on material properties measurements and optical metrology. Digital image correlation utilizes photogrammetry and the terms are used here interchangeably. A brief overview of the principles of operation is presented along with seven sample applications. Material properties measurements utilize

standardized test protocols like ASTM, involving tensile, compression, shear torsional, and biaxial testing. These tests are easily measured with 3D digital image correlation techniques and give full field strain data as well tensile r- & n- values. The 3D digital image correlation technique can be used to evaluate the forming process. The forming limit curve can be automatically created from the 3D DIC system data.

Advantages in deep drawing material testing of the 3D DIC system over standard measuring procedures include high local resolution and small measuring length for determining strain. The only standardized test for yield curve (true-stress vs. true-strain curves) determination is the tensile test. However, the tensile test has a relatively small degree of deformation before fracture because it is uniaxial. Since most industrial forming processes have multi-axial stress states, a hydraulic bulge stretch-drawing test with the 3D DIC can create a strain profile and the creation of the yield curve with a higher degree of deformation (up to 6 times higher) than the tensile test. The multi-axial yield curve does not need the same amount of extrapolation that a tensile test yield curve would need which decreases the amount of uncertainties. A standardized test procedure involving the combined bulge stretch drawing test with the 3D DIC method is being developed and independently verified. The paper summarizes applications of the 3D digital image correlation measurement technique and highlights key experimental set up considerations.

Photogrammetry has been used in other applications, such as in the field of anthropology. Photogrammetry was used in 1995/6 to document the Laetoli hominid

footprint track way, which is a World Heritage site in Arusha, Tanzania[10]. In 2011, Terrestrial laser scan was used to document a portion of the trackway for conservation. The 1995/6 photogrammetry survey utilized digital and film-based cameras and processed the data using standard photogrammetry adjustment. Laser scanning of the trackway and photogrammetric data from the original study showed a high degree of correlation. Surveys were independent of each other and confirmed external accuracy of points of interest on the topography of approximately 0.3 to 0.4mm. Standard deviations that were internal precision measures show an individual point accuracy of 0.1 to 0.2mm.

Photogrammetry is used in the ASTM standard to determining the volume of bulk materials using contours or cross sections ASTM D6172-98 (reapproved 2010) [11]. Two acceptable standard test methods were detailed in this standard to determine the volume of bulk materials using contours and photogrammetric procedures. These test methods are used to determine the volume of bulk materials such as coal or coke piles. Ground mapping and aerial photographs are used with photogrammetric techniques to estimate volume. Photogrammetry quality and procedures for this test standard are referenced to the *Manual of American Society of Photogrammetry* and the *Guidelines for Aerial Mapping*.

The first photogrammetry study conducted on the launch pad was conducted by Littell, Schmidt, Tyson, Oliver, Melis, Ruggeri and Revilock [12], who investigated the stringer cracks in the thermal protection foam on the external liquid oxygen (LO2)

tank, ET 137, of the Space Shuttle STS-133 the November 5th, 2010 scrubbed launch effort. A comprehensive root cause analysis on the stringer cracks was deemed necessary for flight safety before launch could proceed. A tanking test of the external tank, ET-137, with extensive strain gauging, thermocouples, and photogrammetry, was to be carried out. Experimental challenges to implementation included integrating photogrammetry with cryogenically induced deformations of the Intertank-liquid oxygen tank, safety of calibrating photogrammetry cameras in situ, inclement weather, time constraints, as well as the fact that cameras had to be enclosed in nitrogen gas-purged bags to meet safety requirements and mitigate spark, fire, and explosion risk. Mounting the cameras in the test location was also a challenge as thermal distortion of the aluminum or carbon fiber composite support would invalidate calibration. To solve these problems it was deemed safer to calibrate each camera set on the ground and hoist the sets into place instead of in situ calibration, and the aluminum beam was wrapped with a thermal protective blanket to decrease the risk of thermal deflection. Data taken included angular rotation and radial deflection of the LO2 flange. The three-dimensional digital image correlation techniques successfully assisted in determining the root causes of the thermal protection foam stringer cracks. The results, including comparison between photogrammetry data and finite element analysis, full field displacement plots, and extracted data at four points of interest, correlated with significant test time points. It was determined that the fluid level of liquid oxygen strongly influenced the displacements and rotation of the LO2 flange.

3D photogrammetry is a versatile technique to measure strain. It can be applied on a macro and micro scale and has a high degree of accuracy. Important advantages of photogrammetry are that it allows visualization of strain gradients and high stress regions. It can be used to verify and iterate finite element models, and it allows for testing of non-homogeneous and anisotropic materials. These advantages reduce the number of prototypes needed before production. One of the greatest advantages of the technique is that previously "impossible" measurements can be made. Unfortunately, most papers reviewed did not present the full correlation and validation of strain gauges, FEA, and photogrammetry. If the photogrammetric measurements can be correlated to the analytic predictions and strain gage data, these techniques can be used with confidence on the wind tunnel compressor blades. Through the use of photogrammetry, a better understanding of the strains on the complicated shape of the compressor blades may allow for the significant improvement in wind tunnel operation.

1.3 OBJECTIVE

3D Photogrammetry has been shown to be a versatile technique with many applications. NASA Ames has recently acquired a 3D photogrammetry system that is currently undergoing trials to establish confidence among potential users and to determine possible applications. As part of this process, this study intended to validate the strain measurements and to establish a baseline for future use on the aforementioned compressor blade study.

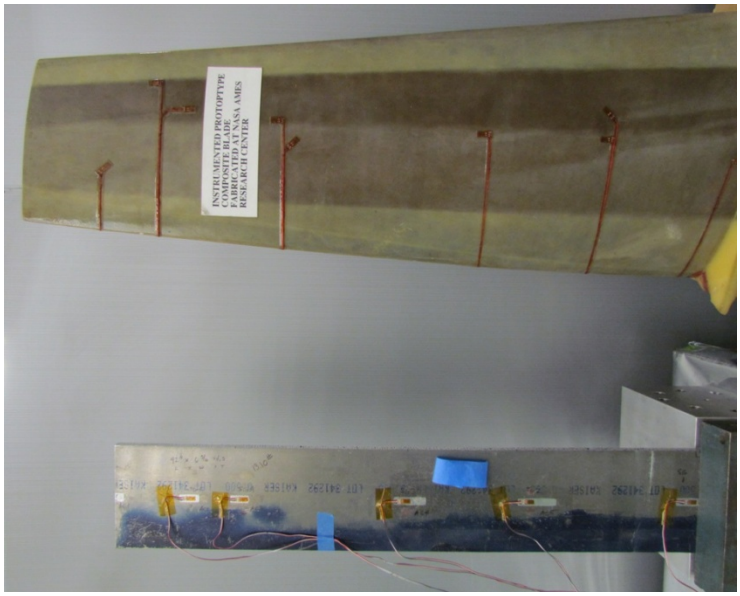

Figure 3 - Compressor Blade with Cantilever Beam

A simple Aluminum 2024-T4 cantilevered beam, shown in Figure 3, was chosen to validate experimentally derived data against classical beam theory. Additionally, finite element models were created to supply further data points. As a first step, the beam was used in a static problem to correlate experimental strain and displacement measures against analytical closed form solutions. Strain was measured experimentally with strain gauges and the 3D photogrammetry system while displacement was measured with a mechanical dial indicator and the 3D photogrammetry system. The second step was to subject the same beam to a dynamic test of the first resonant mode to validate natural frequency. Natural frequency was obtained from displacement, which was derived from the integration of accelerometer data and the 3D photogrammetry system. After the completion of these steps is

accomplished, if the correlation of photogrammetry data is determined to be satisfactory, the same method and techniques can be used with confidence on the compressor blade.

This work will present the results of these tests along with knowledge gained through working with the photogrammetry system and recommendations for future work.

2.0 METHODOLOGY

The material properties of the cantilevered beam are listed in Table 1. Young's modulus for analytical work and FEA analysis was averaged from static and dynamic data. The derivation of static and dynamic Young's modulus are documented in sections 2.1.1 and 2.2.1.

Table 1 - Beam Properties

Material: Al 2024 T4	value (USCU)	unit
Young's Modulus, E	9,580,553	psi
Density, ρ	0.098	lbm/in^3
Poisson's Ratio	0.33	

Total Length, l:	42	in
cantilevered length, L:	35	in
width, b:	6.3125	in
thickness, h:	0.5	in
cross sect area, A:	3.1563	in^2
total weight, W:	13.1	lbf

2.1 STATIC TEST

2.1.1 STATIC TEST ANALYTICAL WORK

The static test consisted of a simple cantilevered beam with applied load from 0 to 50 lbs in 5 lb increments as shown in Figure 4. It was assumed that the beam was ideally fixed.

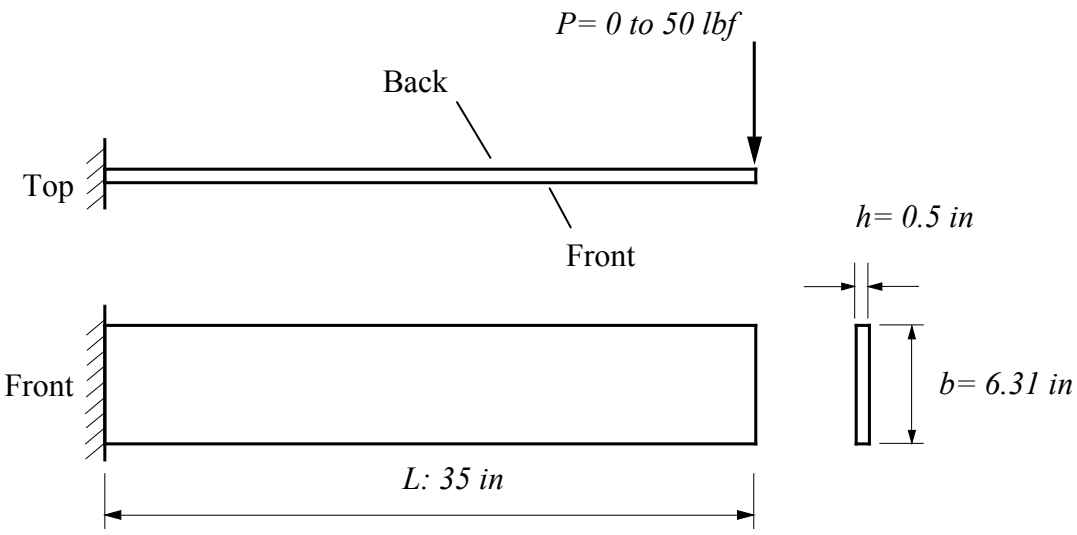

Figure 4 - Static Test, Cantilever Beam

Young's modulus for the static test was determined from an average of experimental data from the LVDT and ARAMIS System. Static Displacement of a cantilever beam can be calculated using the coordinate system shown in Figure 5 and the equation [14]:

$$y(x) = \frac{P}{EI}\left(\frac{x^3}{6} - \frac{L^2 x}{2} + \frac{L^3}{3}\right) \quad \text{(Eq. 1)}$$

where

P: applied load

E: Young's modulus

I: Moment of inertia of the cross section

x: coordinate aligned with the unloaded beam axis with origin at the free end

L: unsupported length

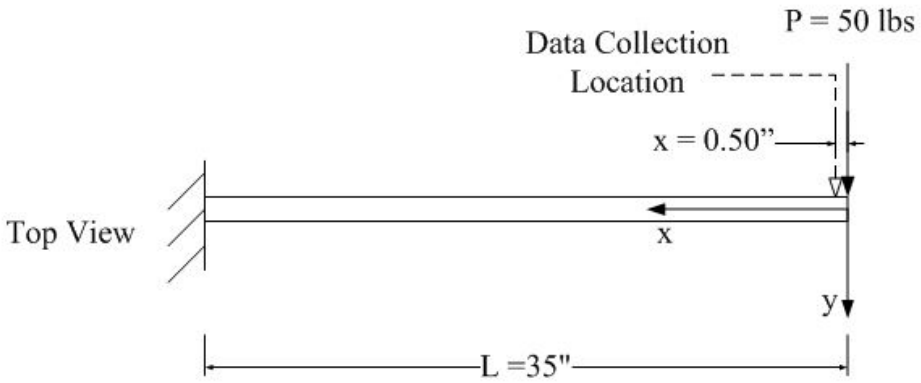

Figure 5 - Analytical Calculation Coordinate System

To determine Young's Modulus, the average experimental displacement at x=0.5 inches is known (y(0.5") = 1.110 in) for P = 50 lbf. Using the following dimensions,

b= 6.312 in

h= 0.5 in

L= 35 in

the cross section's moment of inertia is

$$I = \frac{bh^3}{12} = \frac{6.312\ in\ \times\ (.5)^3}{12} = .0657\ in^4 \quad \text{(Eq 2)}$$

then

$$E = \frac{50\ lbf}{1.110in\ \times\ .0657in^4}\left(\frac{(.5in)^3}{6} - \frac{(35in)^2.5in}{2} + \frac{(35in)^3}{3}\right) = 9{,}580{,}553\ psi$$

(Eq 3)

This experimentally derived Young's modulus (9,580,553 psi) was used in analytical calculations and in the FEA model. Static displacement using this Young's modulus is shown in Table 2.

Table 2 - Applied Load and the Resulting Maximum Displacement

Load, P (lbf)	Analytical Calculated Maximum Displacement (in)
0	0.000
1	0.022
5	0.109
10	0.219
15	0.328
20	0.437
25	0.547
30	0.656
35	0.766
40	0.875
45	0.984
50	1.094

Static Strain was calculated with the equation:

$$\varepsilon = \frac{Mc}{EI} \qquad \text{(Eq. 4)}$$

where

M: Moment

c: Distance from bending axis

E: Young's modulus

I: Moment of inertia

2.1.2 STATIC TEST COMPUTER SIMULATION

2.1.2.1 GENERAL MODEL DESCRIPTION

A CAD model of the cantilevered beam was developed using MSC PATRAN 2011 64-Bit Build 18.9.115609 [15]. This model was analyzed for static loads using MSC NASTRAN 2011.1 [16]. Material properties used were identical to those used in the static analytical work listed in section 2.1.1.

2.1.2.2 BOUNDARY CONDITIONS AND LOADS

The beam was constrained in 6DOF at the end of the beam as shown in Figure 6. Static uniform load was applied in a one-inch area at the tip of the beam. Static loading cases were analyzed for 10, 20, 30, 40, and 50 lbs.

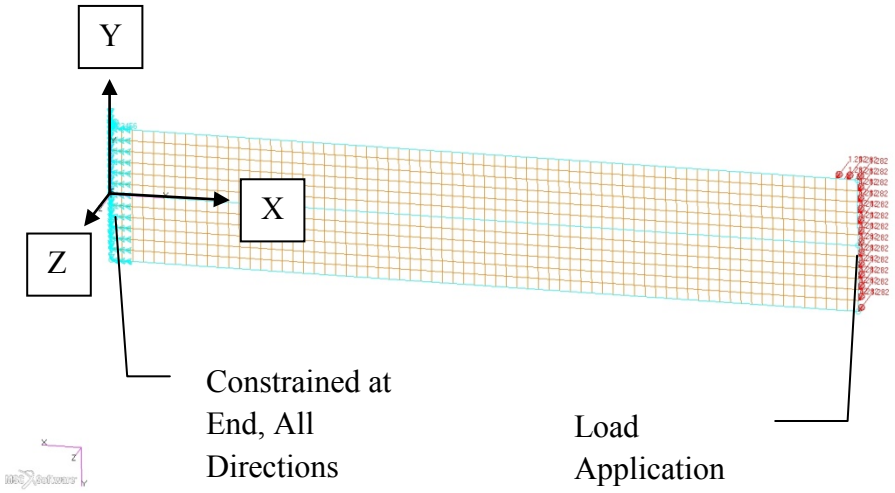

Figure 6 - CAD Model, Static Test Constraints and Load Application

2.1.2.3 FEA MESH CONTROLS

In order to improve the FEA simulation, the element size of the model was constrained to 0.5 inches and is shown in Figure 7. The model geometry was created out of surfaces extruded from the cross sectional curve to ensure data nodes were located at each strain gauge center. Quad (plate) elements were then created from the surfaces and a thickness of 0.5 inches was defined in the material properties. PATRAN element coordinate system is shown in Figure 8 for raw data reference.

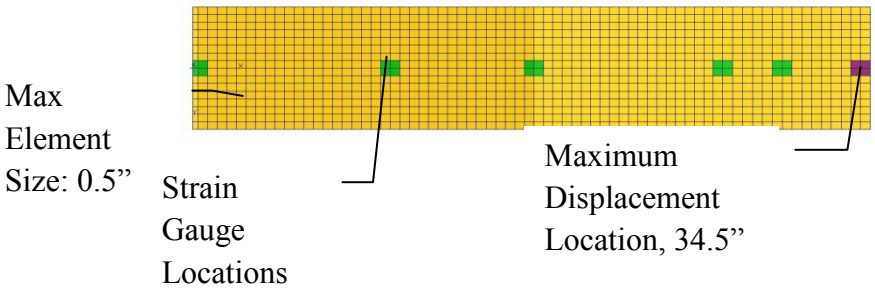

Figure 7 - FEA Model

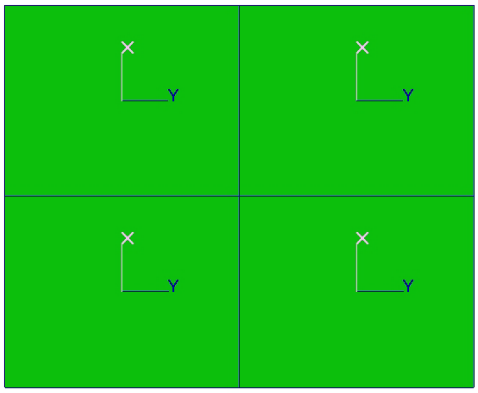

Figure 8 - Element Coordinate System

2.1.3 STATIC TEST EXPERIMENTAL WORK

The aim of the experimental work was to apply static loads and to collect data using traditional strain gauges and the photogrammetry system.

2.1.3.1 STATIC TEST SPECIMEN PREPARATION

The front side of the beam facing the camera was cleaned and covered with regular white matte spray paint until no reflections from the underlying metal was

visible. A stochastic pattern of matte black spray paint was applied on top of the white base coat. The high contrast, randomly generated stochastic pattern was tracked by the ARAMIS software between images and strain was determined from the calculated displacement. Matte paint was critical as glare off the test specimen has the potential to overexpose the photogrammetry system in that part of the data image. Small, consistent sized paint speckles were preferred. Areas without approximately 50% contrasting paint speckles were filled in by hand with a Sharpie brand permanent marker. This however, was not effective as the paint because the ink was reflective and produced a 1-inch hole in the data. The hole in the data did not affect data comparison as it did not occur in areas of critical interest. However, data from surrounding areas was used to interpolate results for these locations to produce a complete full field strain plot. It is recommended that in the future Indian ink be used to augment black speckles to ensure best results.

Strain gauges manufactured by Vishay Precision Group [17] MicroMeasurement (MM) CEA-13-250UW-350, (gage factor is 2.1), were applied in the x-direction at high stress regions of the beam. Surfaces were prepared with Isopropyl alcohol for strain gauge mounting. The blade was strain gauged per Vishay Precision Group Strain Gauge Application Installation Instruction bulletin B-137 [18]. Locations of strain gauges are listed in Table 3 and shown in Figures 9 and 10. Locations were placed close to the first, second, and fifth mode max and to node locations.

Table 3 - Strain Gauge Locations

Location from fixed end (in)	0.275	10.20	17.625	27.375	30.46	35.00
Strain Gauge Channel	1	2	3	4	5	-

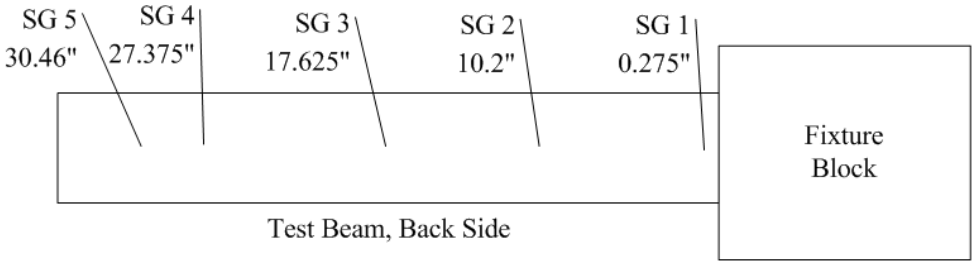

Figure 9 - Strain Gauge Locations Diagram

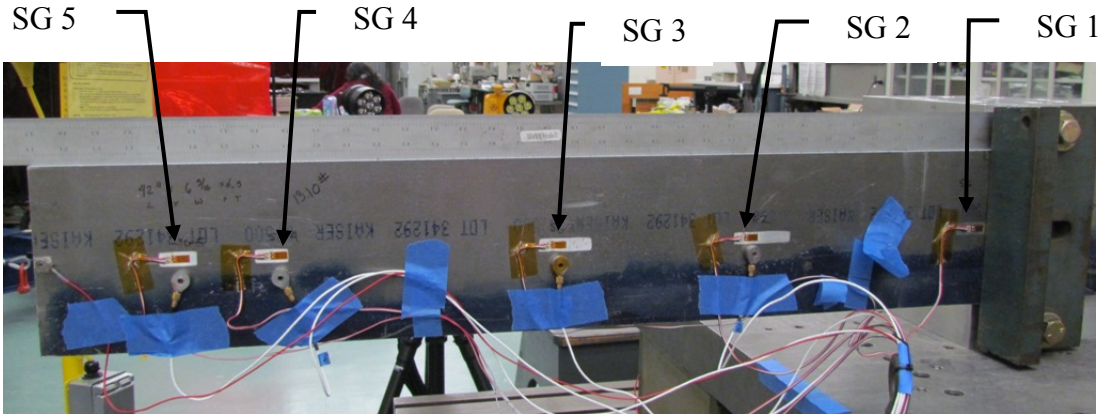

Figure 10 - Strain Gauge Locations, Photograph

2.1.3.2 STATIC TEST PHOTOGRAMMETRY

This study used a 3D Digital Image Correlation system, the ARAMIS - Optical 3D Deformation Analysis 12M System produced by GOM (Gesellschaft für Optische Messtechnik) International AG [20], which utilizes photogrammetry to determine displacement. Strain data are derived from displacement information. The photogrammetry cameras are shown in Figure 11. Strain measuring range published by the company is 0.01 to> 100 % and the strain measuring accuracy is up to 0.01% [20].

Figure 11 - ARAMIS System by GOM, Digital Cameras and Illumination System

The photogrammetry system was calibrated using the CC20 Calibration object shown in Figure 12. The calibration step was critical to data collection with this system because it detected the exact location and view angle of the two cameras. The calibration step not only informs the sensor where the hardware is in relation to one

another, it accurately relates the left and right camera images to one another in the software and . A screen shot of a sample calibration result in front of the left and right camera images are shown in Figure 13. The calibration test object is a precision piece that is positioned a known distance from the camera and oriented in specified ways so the software can detect the cameras' locations. The calibration step also establishes a volume in which test objects can be detected accurately by the system.

Figure 12 - ARAMIS Calibration object

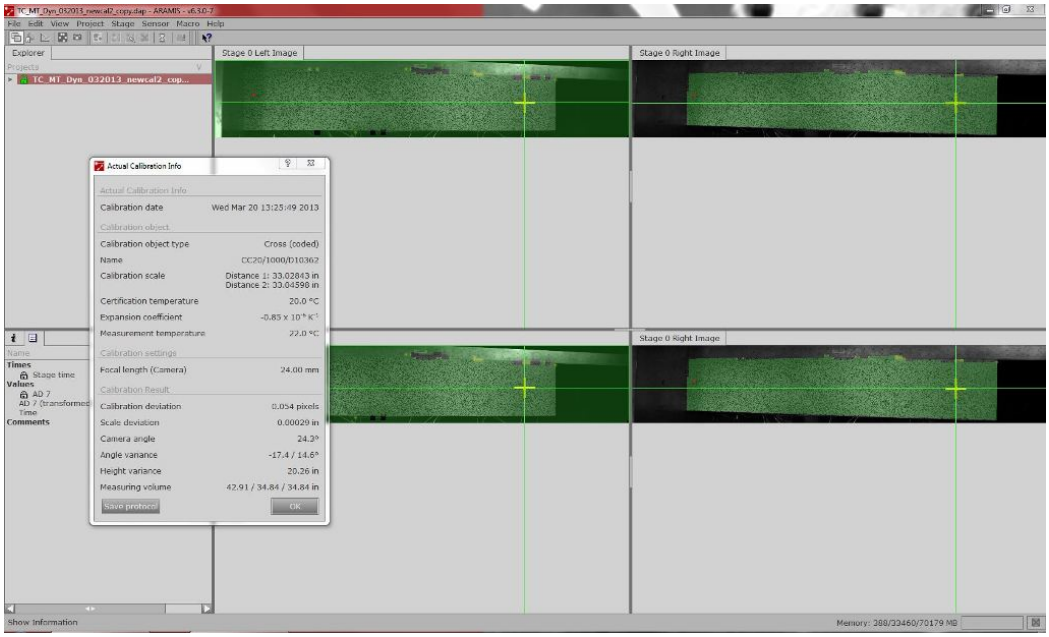

Figure 13 - Sample Calibration Result and Left & Right Camera Images

2.1.3.3 STATIC TEST SET-UP

A 70 lb aluminum block was fabricated to mount the cantilever beam to a static base fixture as shown in Figure 14. A steel backing fixture was used to bolt the cantilever beam to the aluminum block. Bolts were placed at four points in and around the beam. Brass shim stock .002 inches thick was placed at the front and back edges of the beam to ensure no beam rotation was present inside the fixture.

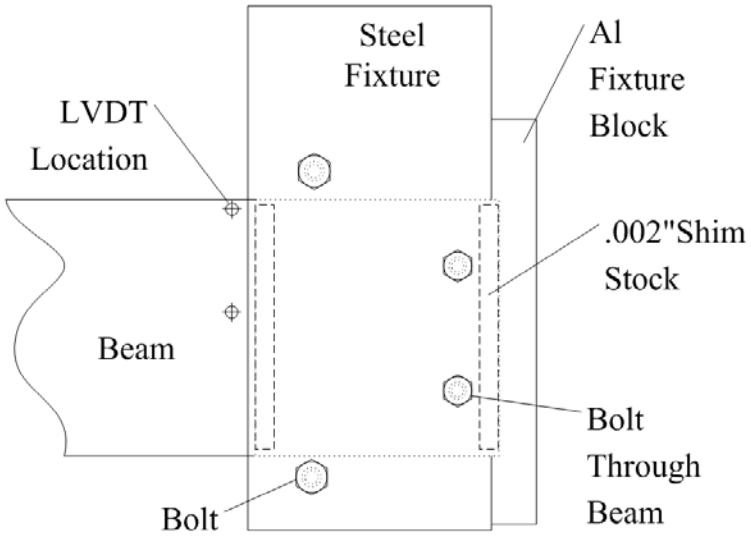

Figure 14 - Fixture diagram

LVDT's were placed .25 inches from the fixed end at the top and middle of the beam to monitor the displacement near the fixture. Maximum displacement of .0003 inches was found at the top of the beam and .001 inches was found at the middle of the beam during 50 lb loading. Analytically the expected displacement for this location at 50 lbs should be 0.000085 inches. While there was still more movement than expected at this location, the displacement at the fixed end in previous fixture configurations before efforts were made to increase fixture stiffness was as high as .00215 inches at the top and .0025 inches at the middle location.

A diagram of the static test set-up is shown in Figure 15. Photographs of the test set-up are presented in Figures 16 and 17. Load was also applied from the back side on a load distribution block with a locating dimple to ensure centered load application, as shown in Figure 18.

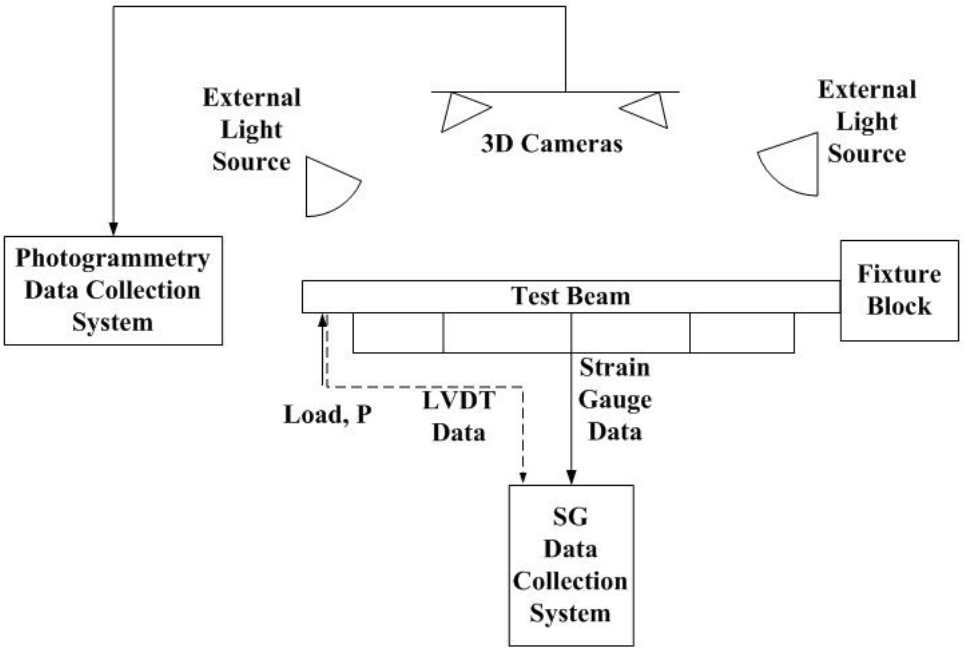

Figure 15 - Static Test Set-up Diagram

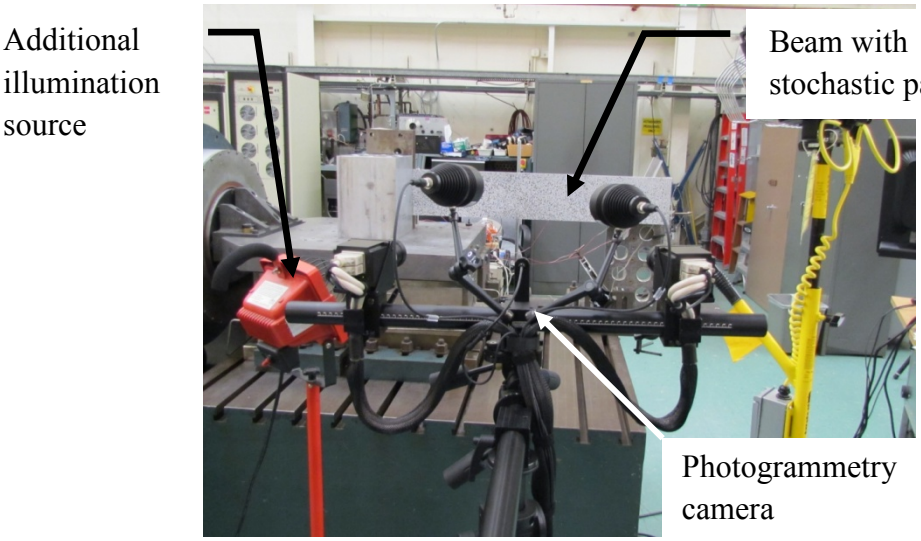

Figure 16 - Static Test Set up, Front

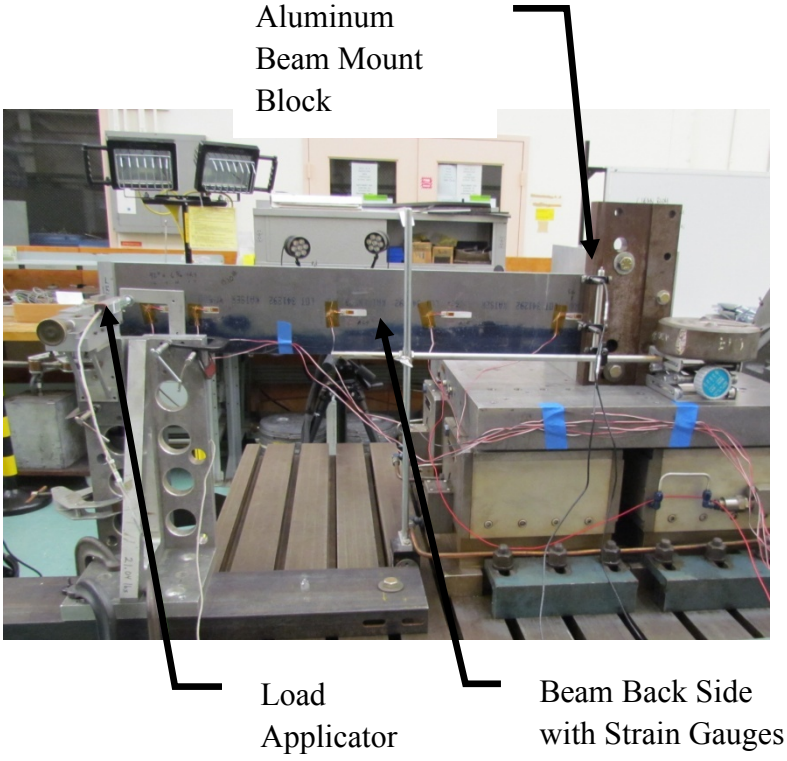

Figure 17 - Static Test Set up, back side

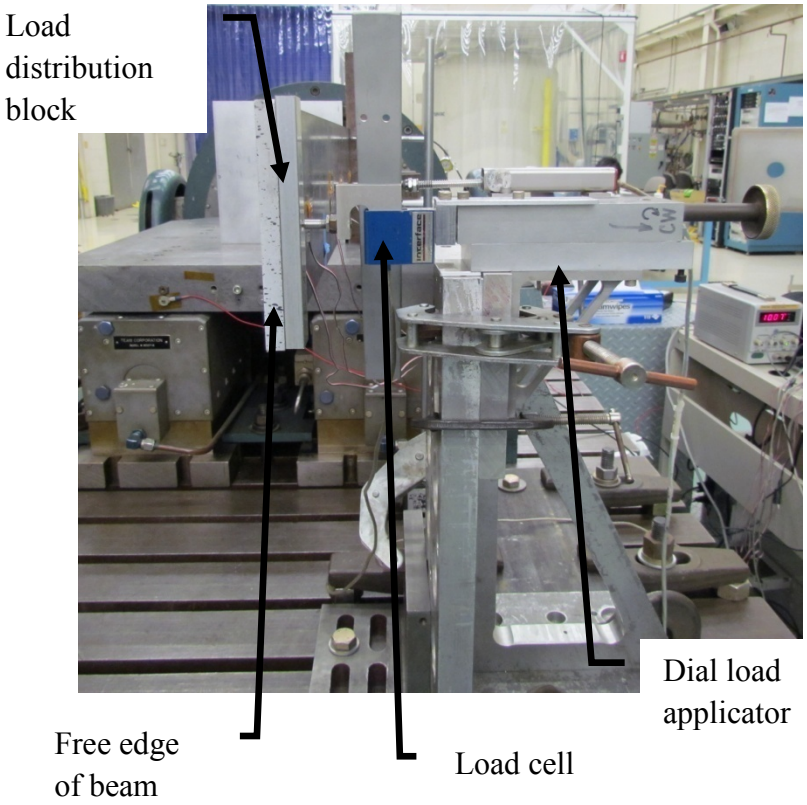

Figure 18 - Static Test Set up, Free Edge, Beam axis into the page

Static load was applied at 5 lb increments up to 50 lbs. Strain gage data was taken continually. Displacement was read off the LVDT and photogrammetric data was taken once the load stabilized. LVDT, load cell, and signal conditioner information is documented in Appendix A.

2.1.4 STATIC TEST RESULTS AND CORRELATION

2.1.4.1 STATIC DISPLACEMENT

Maximum displacement data from the static load tests are shown in Table 4 and represented graphically in Figure 19. All displacement comparisons were for the 34.5 inch location on the beam. Eight static load tests were completed. Photogrammetry and LVDT displacement data were obtained for all trials. FEA Displacement data were analyzed only for load cases 10, 20, 30, 40, and 50 lbs.

Table 4 - Static Load Data

Load, P (lbf)	Analytical Calculated Max Displacement, at 34.5(in), E= 9.72e6	LVDT Average at 34.5(in) n=8	FEA simulation Displacement at 34.5(in), E=9.72e6 psi	ARAMIS Average, 34.5 (in), n=8
0	0.0000	0.0003	0.0000	0.0001
1	0.0219	0.0258	-	0.0217
5	0.1094	0.1208	-	0.1096
10	0.2187	0.2354	0.2152	0.2196
15	0.3281	0.3493	-	0.3297
20	0.4375	0.4604	0.4305	0.4392
25	0.5469	0.5719	-	0.5498
30	0.6562	0.6817	0.6457	0.6606
35	0.7656	0.7925	-	0.7707
40	0.8750	0.9013	0.8609	0.8810
45	0.9843	1.0110	-	0.9902
50	1.0937	1.1196	1.0762	1.1003

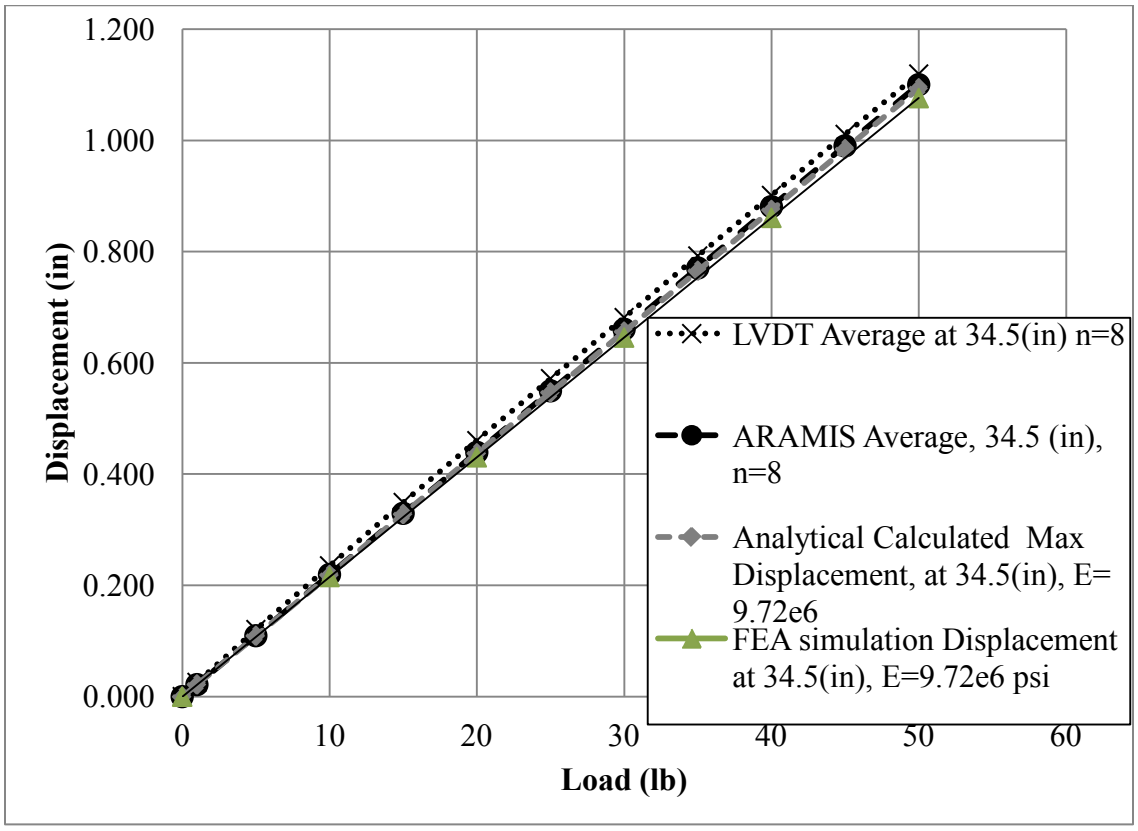

Figure 19 - Static Test Maximum Displacement vs. Load

Table 5 - Maximum Displacement Percent Deviation from Analytical Calculation

Load, P (lbf)	% (Analytical-LVDT Ave)/ Analytical*100	% (Analytical-FEA)/ Analytical*100	% (Analytical-ARAMIS Average)/ Analytical*100
0	-	-	-
1	-17.978	-	0.709
5	-10.478	-	-0.229
10	-7.618	1.605	-0.407
15	-6.444	-	-0.469
20	-5.238	1.605	-0.403
25	-4.579	-	-0.545
30	-3.883	1.605	-0.669
35	-3.508	-	-0.672
40	-3.006	1.605	-0.687
45	-2.713	-	-0.599
50	-2.366	1.605	-0.605
Average	-6.165	1.605	-0.416
SDV	4.608	0.00001	0.399

Beam maximum displacement percent deviations from analytical calculations are presented in Table 5. Average deviation from analytical for the LVDT was -6.165% with a standard deviation of 4.608%. Average deviation of analytical from FEA model was 1.605% with a standard deviation of 0.00001%. Average deviation from analytical of the ARAMIS system was -0.416% with a standard deviation of 0.399%. Percent deviation decreased for LVDT as load increased indicating higher reliability at higher loads. At 1 lb, LVDT percent deviation was -17.987%, and at

50 lbs percent deviation was -2.366%. The LVDT was mounted on the strong back, which was clamped onto a cantilevered beam toe-clamped to ground. It is suspected that this assembly could be stiffened to improve results.

2.1.4.2 STATIC STRAIN

Static strain values were recorded using strain gauges and the photogrammetric system. Strain gauges recorded strain data in mV and was converted to strain with the following equation:

$$Epsilon = \frac{4(SG\ mV - SG\ mV_{initial})}{(Active\ Leg \times Gauge\ Factor \times Input\ Power\ V)} \times \frac{1\ V}{1000\ mV} \quad \text{(Eq 5)}$$

where

Active leg = 1

Gauge Factor = 2.1

Input Power = 10 V

A typical example of FEA Strain results is presented in Figures 20 and 21 for the 50 lbs load case. In Figure 21, strain increases linearly along the length of the beam towards the fixture. The peak at the fixed end is consistent with modeling singularities

that occur from transitioning from fully fixed constraint elements to elements allowed to move. This high stress singularity is an artifact of the FEA process and can be ignored. If element size were increased, this artifact would disappear.

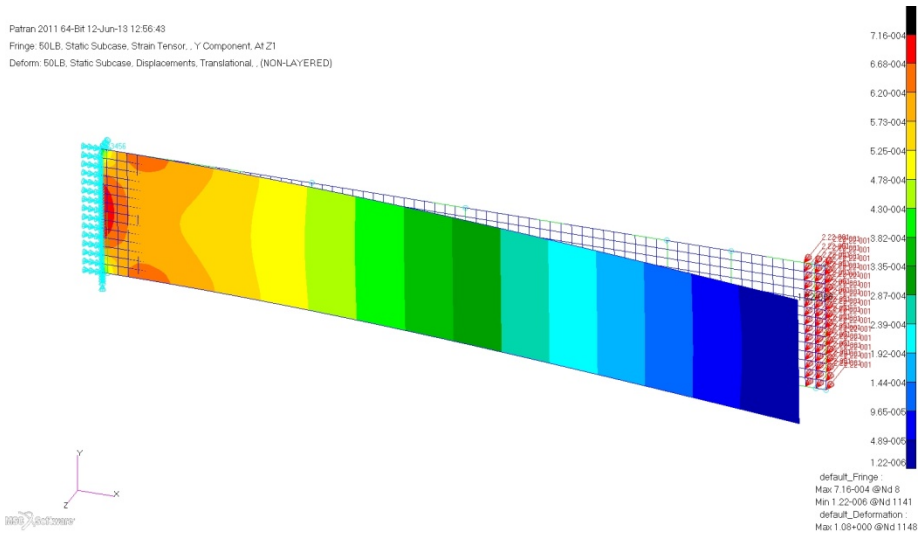

Figure 20 - FEA Epsilon X Strain Fringe Plot 50 lbs, Deformed

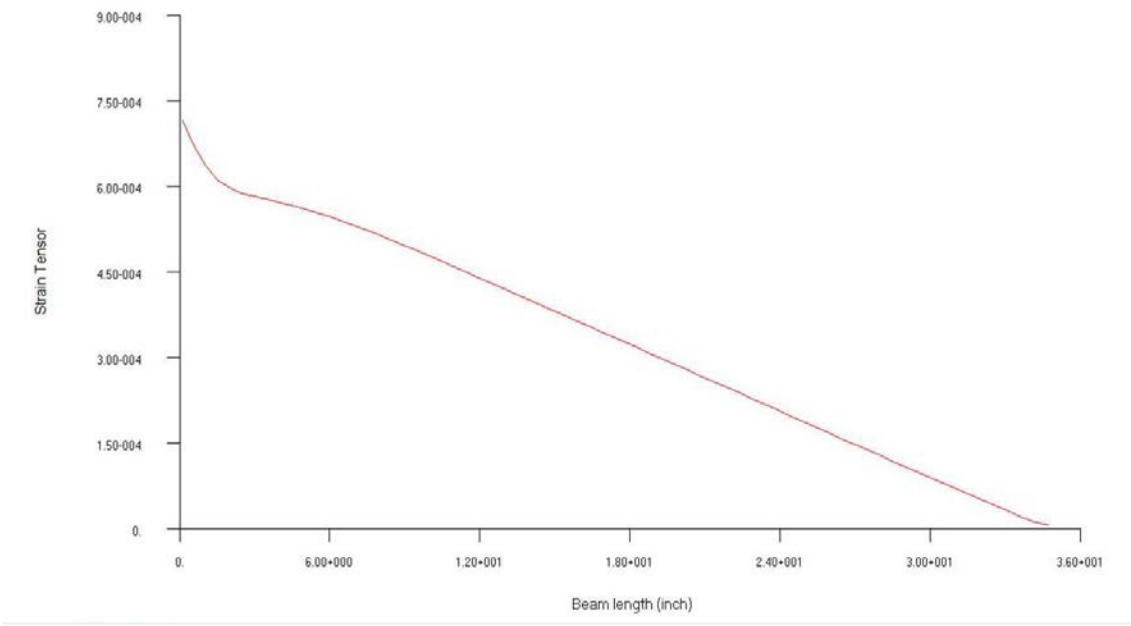

Figure 21 - FEA Strain at Midline, X-Direction

A sample of a semi-automatically generated photogrammetry report is included in Figure 22 depicting the 50 lb load case for one test (file name TC_MT_060313_FixedFixt1). Similar reports can easily be generated by the ARAMIS system for displacement data.

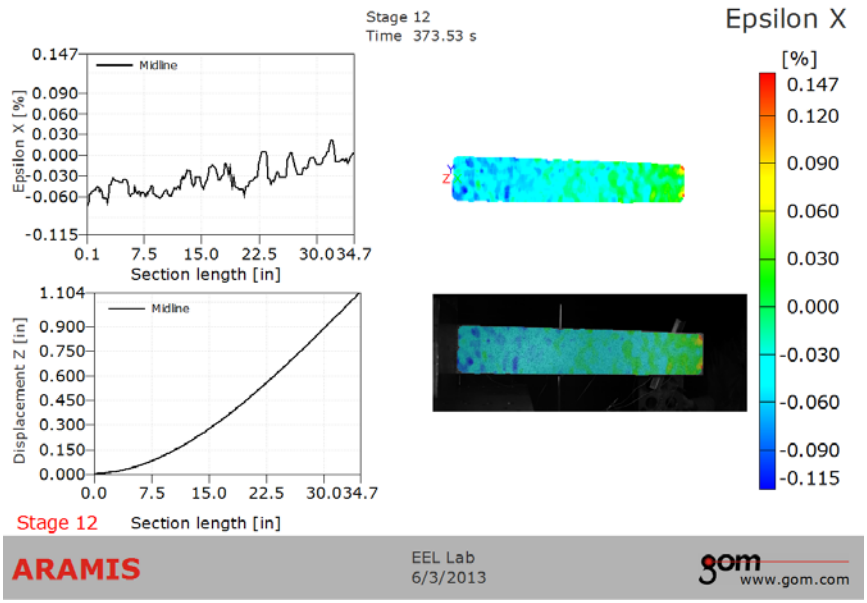

Figure 22 - Sample Photogrammetric Displacement & Epsilon X Strain Results, 50 lbs

Photogrammetry x-direction (Epsilon X %) full field strain plots are shown in Figures 23 through 28 for load conditions 0 through 50 lbs in ten pound increments for the same test.

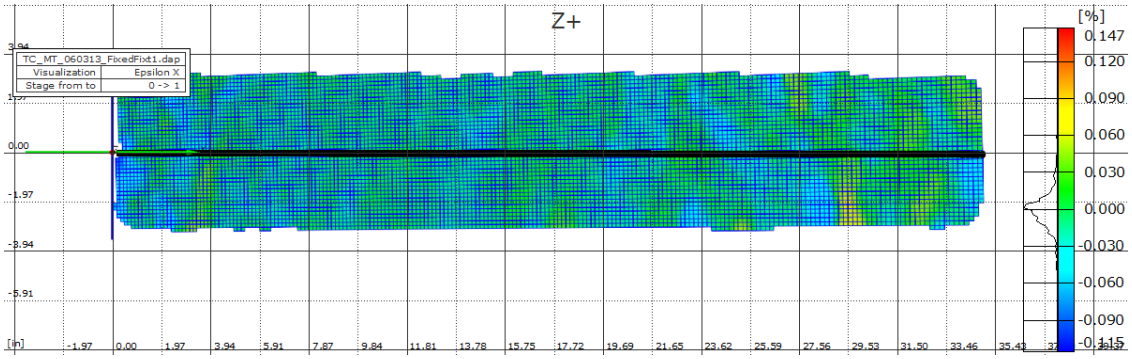

Figure 23 - Full Field Strain Plots, 0 lbs Noise Test

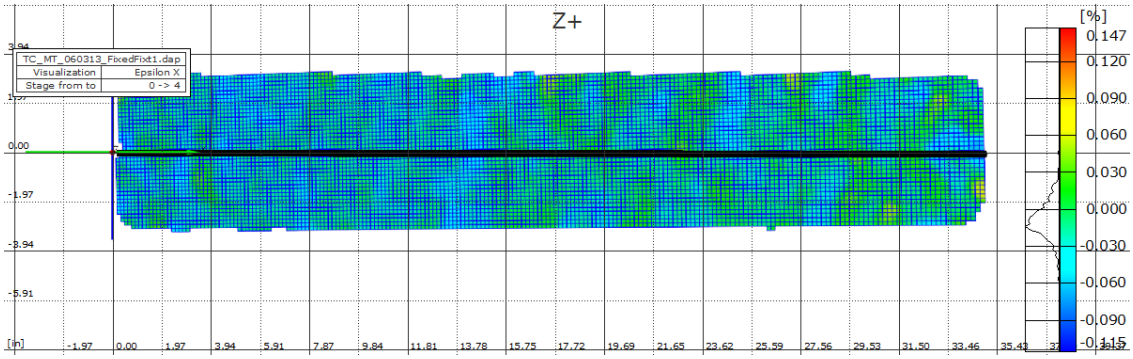

Figure 24 - Full Field Strain Plot, 10 lbs

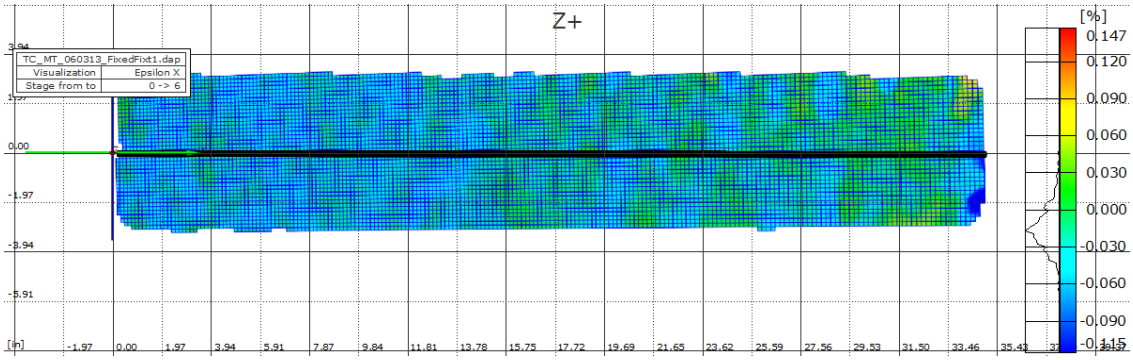

Figure 25 - Full Field Strain Plot, 20 lbs

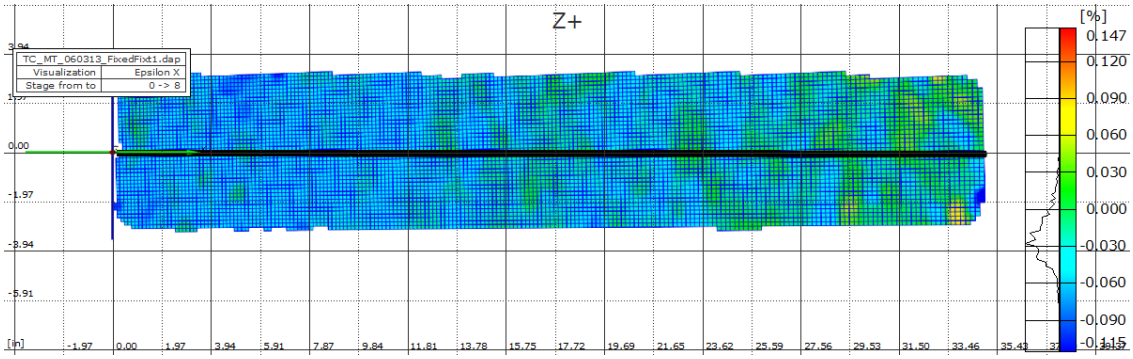

Figure 26 - Full Field Strain Plot, 30 lbs

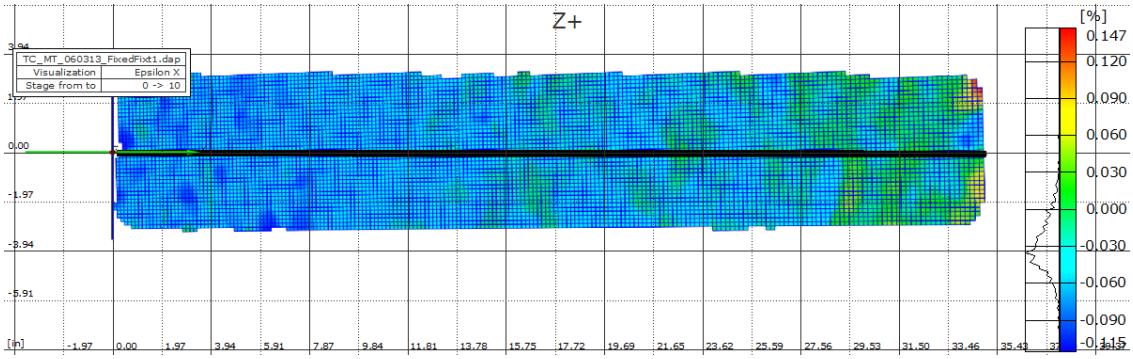

Figure 27 - Full Field Strain Plot, 40 lbs

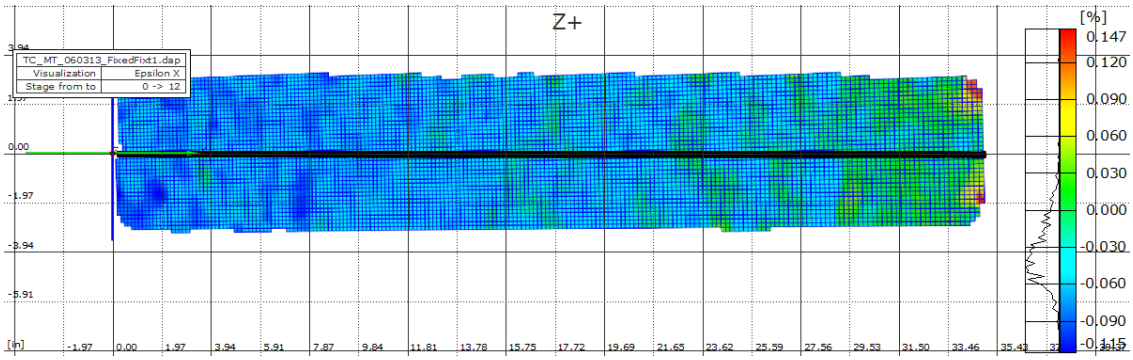

Figure 28 - Full Field Strain Plot, 50 lbs

The results of the full field strain plots show actual strain over the majority of the beam. However, currently, the ARAMIS system is not capable of averaging the full field strain plots from a number of tests into one average full field strain display. In order to obtain the average strain of a number of trials, only strain gauge locations were selected for comparison.

A section was created along the midline of the beam to display Epsilon X strain along the midline. A semi-automatically generated graph of strain along that midline section for all load conditions of one test is shown in Figure 29, with the 0 lbs load case marked in red.

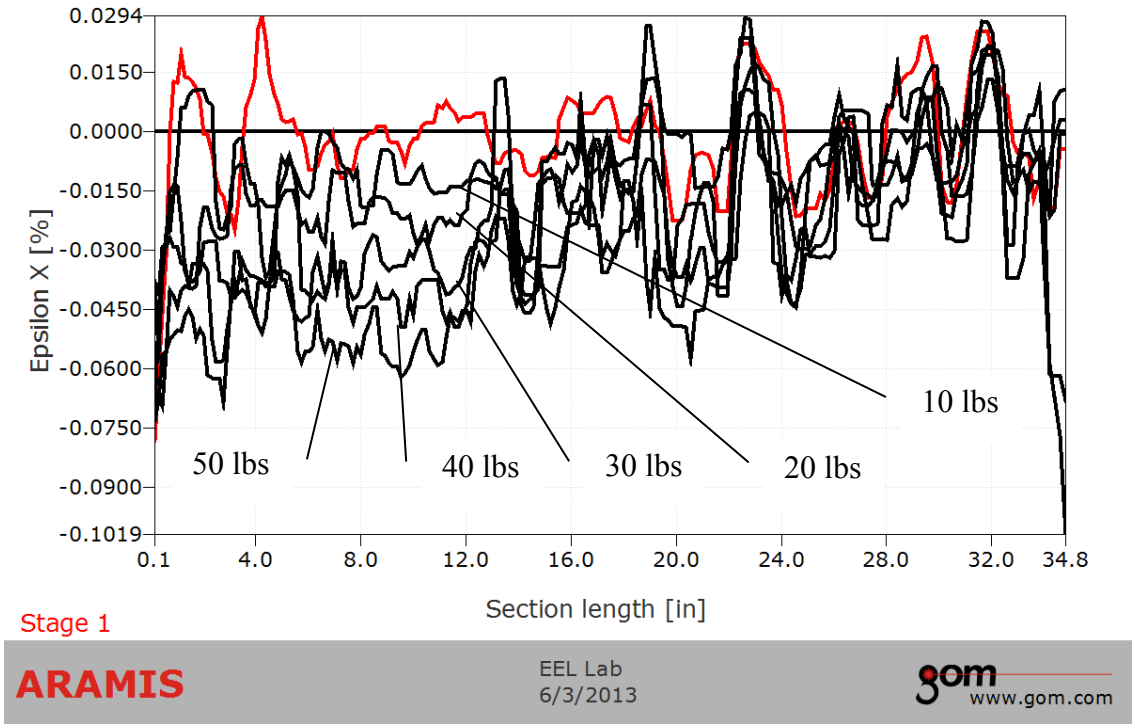

Figure 29 - Photogrammetry Strain vs. Section length, All load cases

The midline section data for the 50 lb load case for one test was extracted from the photogrammetry system as a text file and imported into MS Excel. The data was graphed and shown in Figure 30. The y-axis was inverted for ease of comparison with the FEA midline strain graph shown in Figure 21. Photogrammetry strain data is

presented as percent strain, so the numbers must be divided by 100 to account for the difference in units and multiplied by -1 to correct for differing coordinate systems.

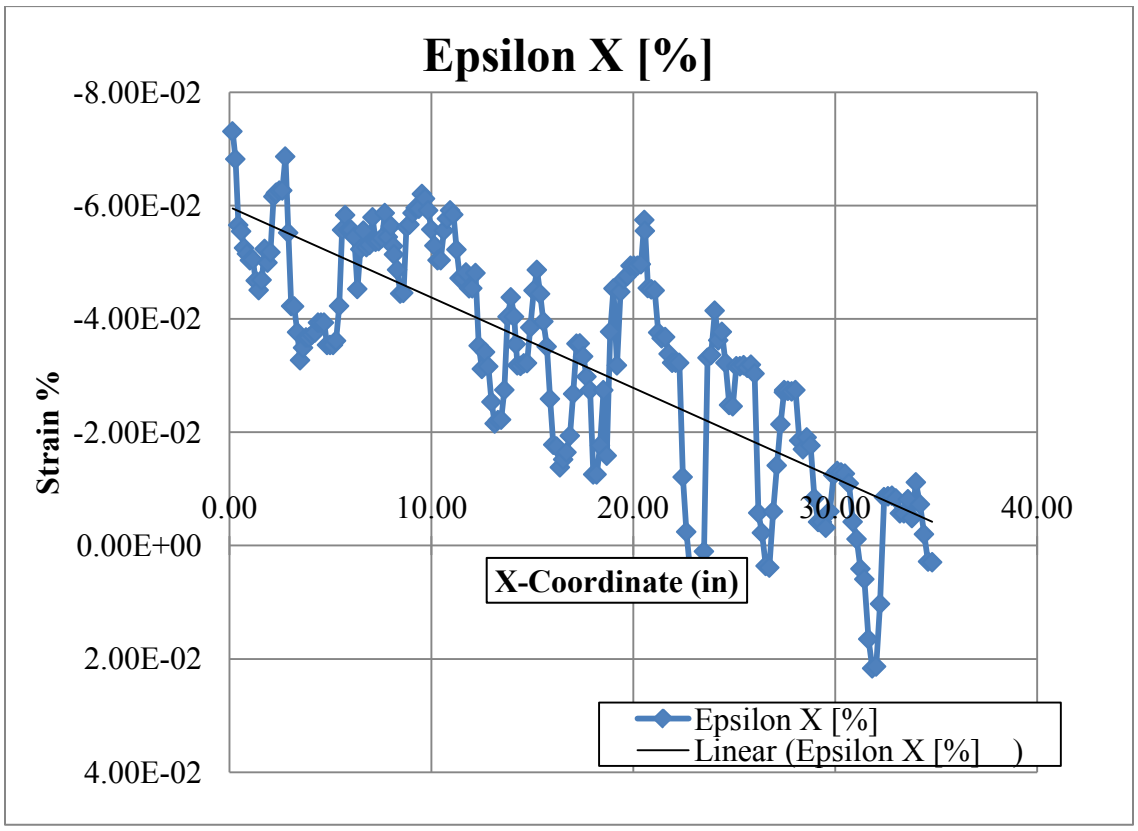

Figure 30 - Photogrammetry Midline Strain, 50 lb load case

It can be seen from Figures 30 that actual strain values of the test specimen along the midline vary considerably in just one load case. This is may be due in part to actual variations in the material. However, there may be a significant signal-to-noise effect that confounds the actual strain data for any one point or section line examined.

The company that produces the ARAMIS system recommends a baseline noise test be carried out before testing. The recommended signal to noise ratio for valid data is ten times the noise baseline. The signal-to-noise ratio was not explored in this study but could potentially explain why strain deviation from analytical was high. It can be seen in Figure 29, at strain gauge 1 location the 0 lb case (noise baseline) is very high, and the signal-to-noise ratio between noise baseline and the 50 lb case is 1.16 which indicates that the data is influenced by noise. At strain gauge locations 2 and 3, the signal-to-noise ratio between noise baseline and the 50 lb case is 4.91 and -6.26 respectively which would contribute to why data at these locations have a lower deviation from analytical as shown in Figures 31-35.

Improvements on the signal-to-noise ratio could be as simple as increasing the lighting in high noise areas to improve the contrast between the speckle pattern and white background, increasing shutter speed to allow more light in to the camera sensor, increasing facet and step size used in the computation of strain, or increasing the strain validity quote which would decrease the tolerance to edge noise. Other more involved improvements for the signal-to-noise ratio could include decreasing speckle size or increasing the loads applied to the test object to ensure the strain level tested has a high signal-to-noise ratio. An average of the data or a best fit line may more accurately correspond to the actual strain. The linear trend line resembles expected strains predicted in the FEA analysis.

To obtain exact comparisons between photogrammetry results, FEA, strain gauges, and analytical results, seven photogrammetry trials were analyzed. One trial was thrown out due to abnormal strain readings. Data from only strain gauge locations were analyzed for all conditions by averaging the data spanning the length of the strain gauge. The averaged strain comparison results for selected loads are summarized in Figure 31-35. ARAMIS data that falls below the lower capability of strain detection (0.0001 in/in) is marked by an unfilled red triangle and should be disregarded.

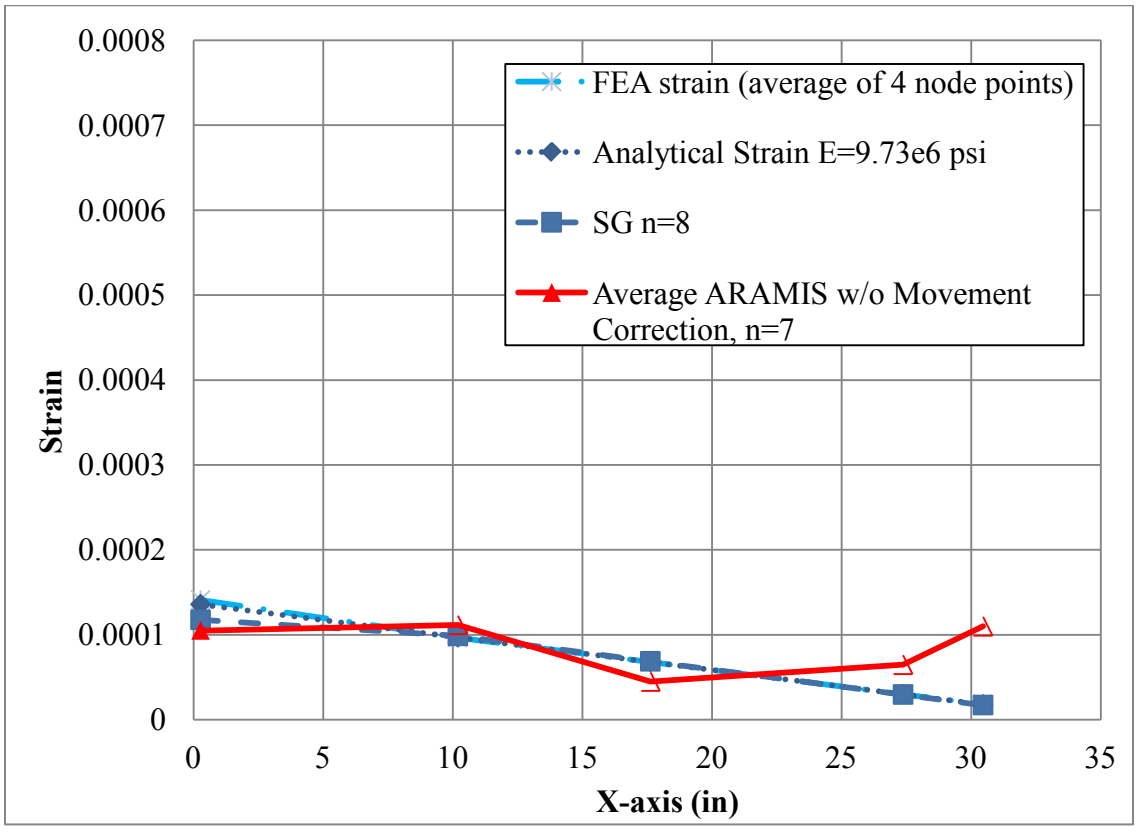

Figure 31 - Static Test, Strain vs. X-coordinate, 10 lbs

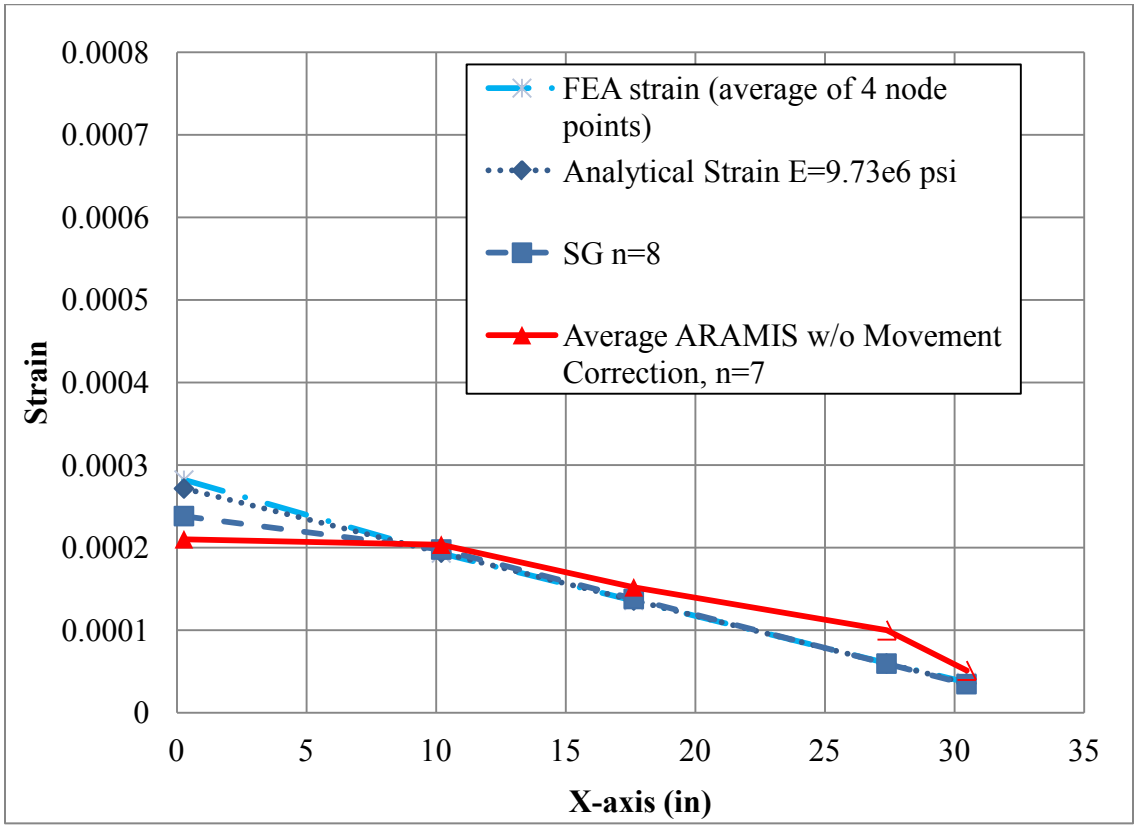

Figure 32 - Static Test, Strain vs. X-coordinate, 20 lbs

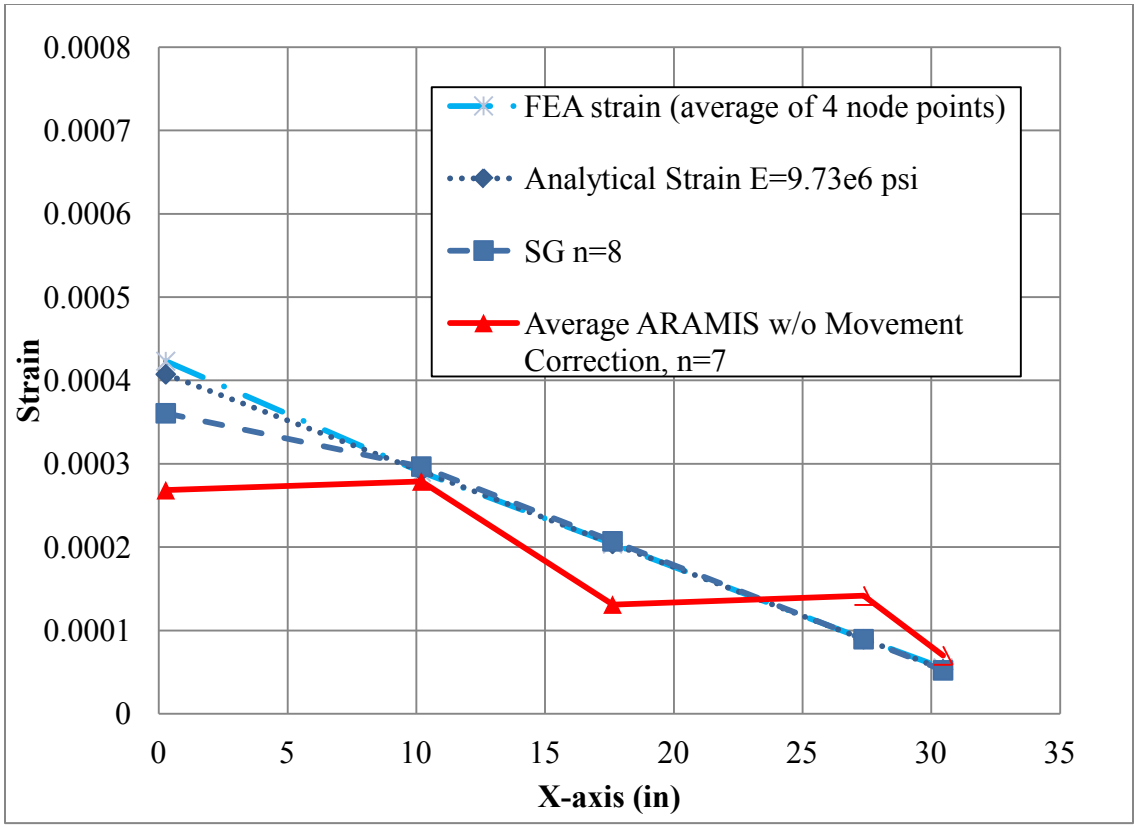

Figure 33 - Static Test, Strain vs. X-coordinate, 30 lbs

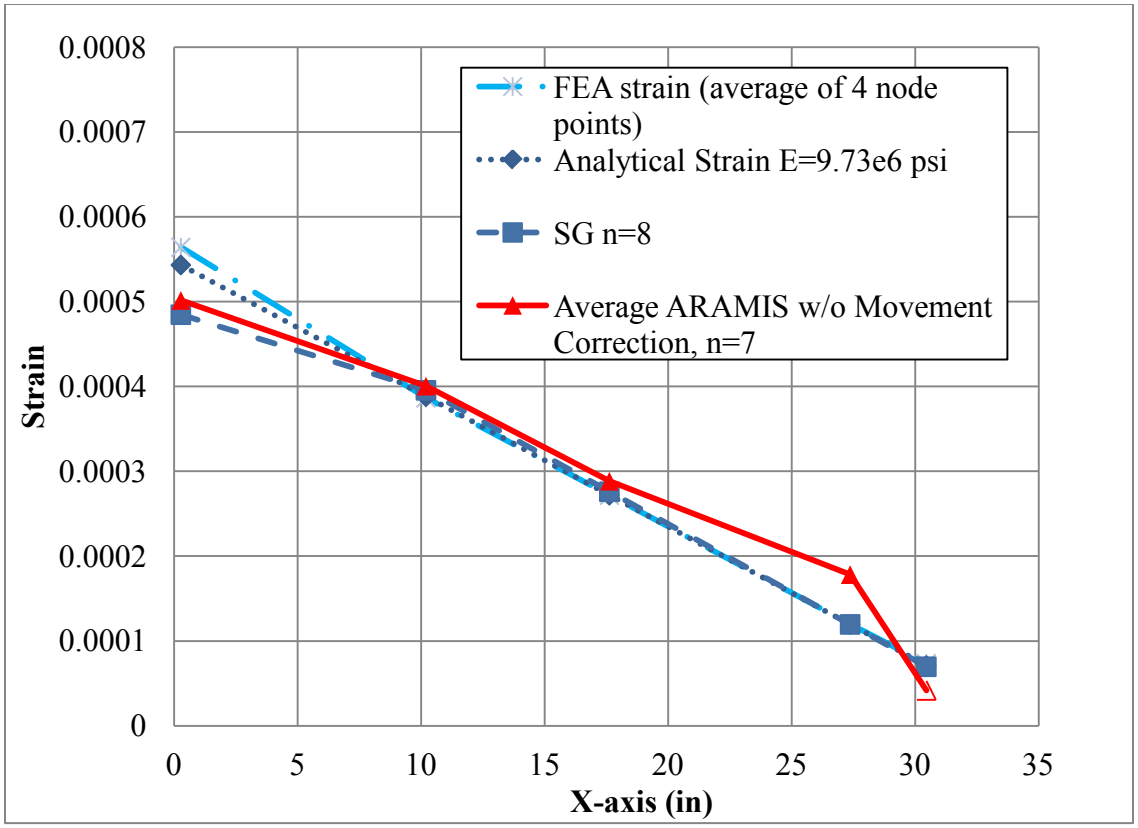

Figure 34 - Static Test, Strain vs. X-coordinate, 40 lbs

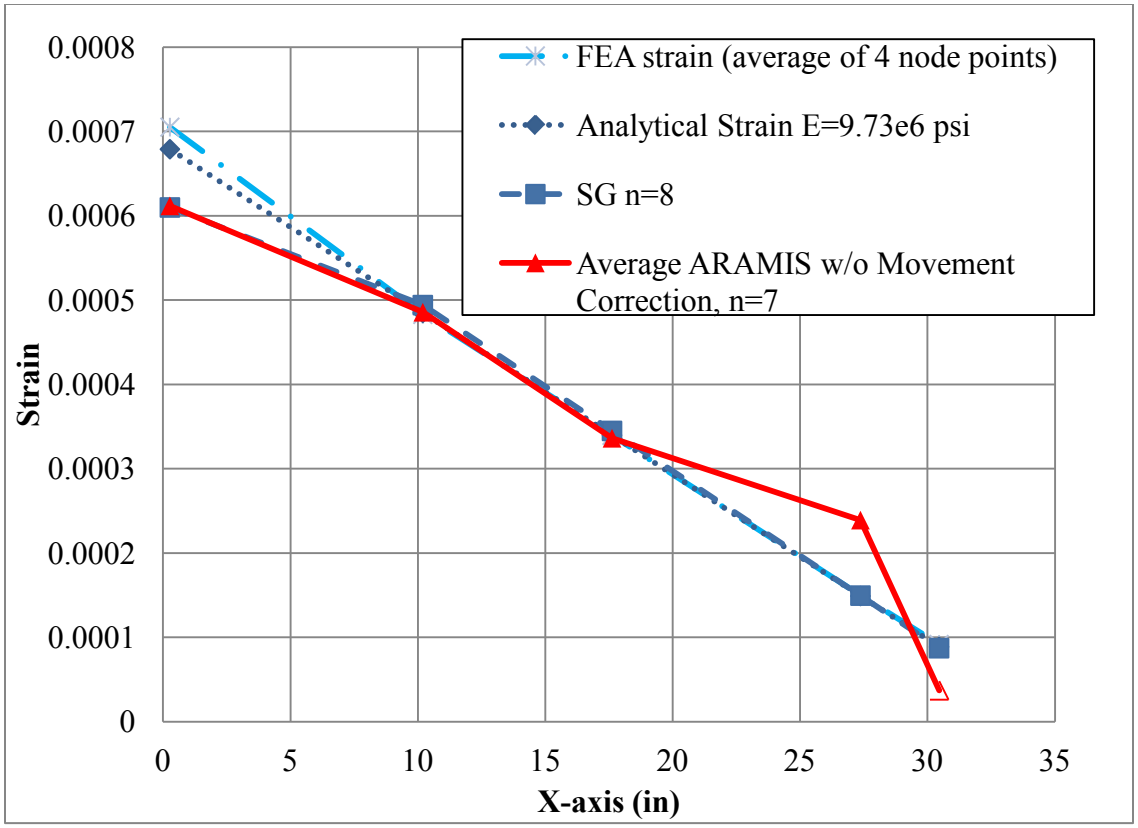

Figure 35 - Static Test, Strain vs. X-coordinate, 50 lbs

The percent deviations from analytical calculations are shown in Table 6 with invalid data removed.

Table 6 - Strain Percent Deviation from Analytical

Load, P (lbf)	SG #	SG center (from fixed end) (in)	%(Analytical-SG)/Analytical * 100	%(Analy-FEA)/Analy * 100	%(Analy-ARAMIS)/Analy * 100
10	1	0.275	13.38	-3.85	22.68
10	2	10.2	-1.66	0.39	-
10	3	17.625	-1.04	0.04	-
10	4	27.375	0.87	-0.49	-
10	5	30.46	3.48	-3.26	-
20	1	0.275	12.29	-3.85	22.62
20	2	10.2	-1.92	0.39	-4.98
20	3	17.625	-1.41	0.04	-11.80
20	4	27.375	0.24	-0.49	-
20	5	30.46	2.57	-3.26	-
30	1	0.275	11.48	-3.85	34.14
30	2	10.2	-1.95	0.39	4.19
30	3	17.625	-1.51	0.04	35.70
30	4	27.375	-0.01	-0.49	-
30	5	30.46	2.26	-3.26	-
40	1	0.275	10.78	-3.85	7.69
40	2	10.2	-1.94	0.39	-3.20
40	3	17.625	-1.53	0.04	-6.07
40	4	27.375	-0.19	-0.49	-49.39
40	5	30.46	2.00	-3.26	-
50	1	0.275	10.18	-3.85	9.90
50	2	10.2	-1.89	0.39	-0.14
50	3	17.625	-1.52	0.04	1.05
50	4	27.375	-0.32	-0.49	-60.38
50	5	30.46	1.78	-3.26	-

The lowest strain that the ARAMIS sensor can detect is 0.0001 in/in with a resolution of $50x10^{-6}$ in/in. Because a cantilever beam is being measured, there is no strain at the tip. The beam has less curvature at the tip than in the middle as shown in the FEA model in Figure 36. The strain decreases below 0.0001 in/in in areas closer to the free end, and data cannot be accurately collected below this threshold. It can be assumed that photogrammetry data at the strain gauge 5 location (30.46 inches) is not valid for any load cases. The lower limit in strain detection for each test set up is determined by the noise baseline.

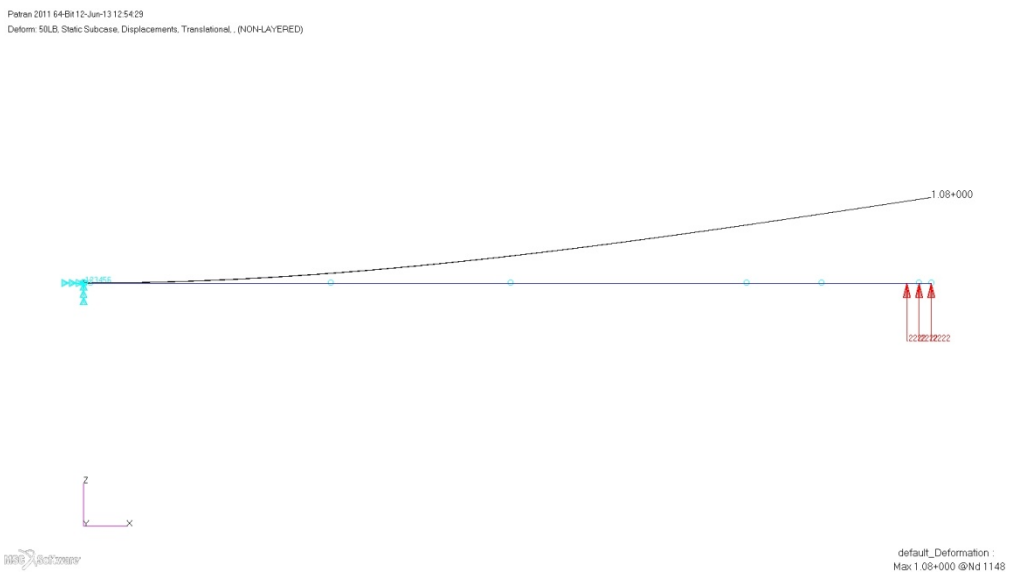

Figure 36 - Beam curvature, FEA Displacement 50 lbs, Side View

Analytical strain for the load case for 10 lbs is above the lower limit for strain detection in the area between 0 and 9 inches from the fixed end. This implies that only strain gauge 1 is valid for this load case.

The static strain comparisons shown in Figure 31-35 are less conclusive than that of the displacement results. Disregarding data known to fall outside of the strain detection capabilities of the ARAMIS system, strain roughly follows the same trend line. At strain gauge 1, where highest strain is expected, in all except for the 30 lb case, there is a strong correlation between the two experimental data sets and the two analytical data sets, but between the experimental and analytical groups the correlation is weaker. All photogrammetry data for the 30 lb load case was re-examined but no processing errors were detected and no test notes could be found that might explain why this data follows a different trend than other load cases.

Strain is a value derived from displacement information. Displacement data had an acceptable percent deviation, but are calculated from the 3D coordinates from the contrasting pixels of the stochastic pattern. Any noise in the displacement data would be carried through calculations and be more pronounced in strain values. Strain deviation from analytical was as high as -61% for 50 lbs at the strain gauge 4 location.

A small factor that may play into strain deviation from analytical results is that in-plane displacement accuracy is 3 times better than out-of-plane accuracy. In-plane displacement sensitivity is reported by the company to be 15 microns at 1 meter x 800 mm field of view. The in-plane strain sensitivity is of 50×10^{-6} in/in. Care must be

made during test configuration to ensure critical strains are measured in-plane if strains measured are close to these published limits.

A strain gauge averages strain over the area to which it is affixed. The photogrammetry data used in Figures 31-35 is an average of only 14 points of strain data for each strain gauge location. However, one of the benefits of the ARAMIS system is that much more data is collected than is represented in Figures 31-35. The photogrammetry data for the 50 lb load case along the midline of the beam for seven tests were averaged together to create one representative curve shown in Figure 37 indicated by a solid blue curve. It overlays the existing data for the 50 lb load case along with a linear curve fit of the average photogrammetry data, $y(x) = -0.000015x + 0.000609$. Photogrammetry data below the known strain sensor limitation was excluded.

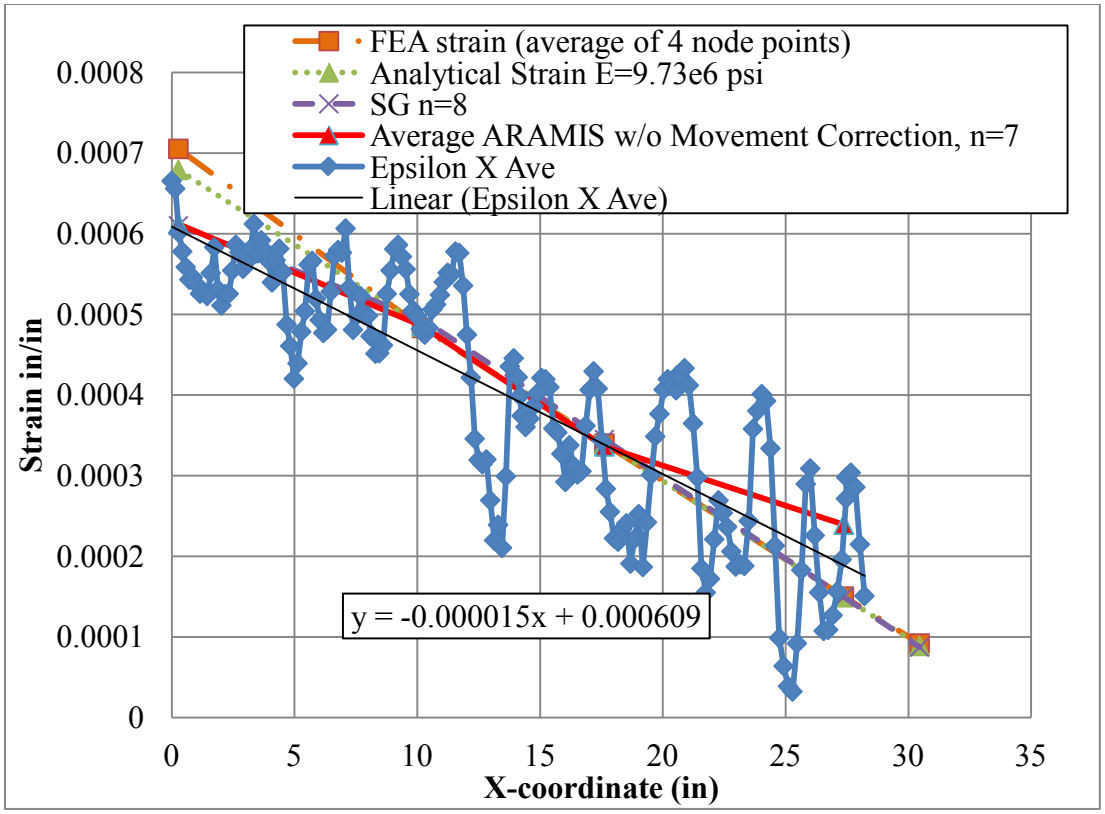

Figure 37 - Photogrammetry Strain, 50 lbs with Average Photogrammetry Data Overlay

Figure 37 shows how the average photogrammetry data along the midline relates to the analytical data. It was hypothesized that by including more data from the rest of the midline, the linear curve fit would better match the analytical curve. However, this linear fit curve does not have the same slope as the analytical results. Unlike strain gauges, the photogrammetry data represented in this curve is a single line instead of an average strain over an area. It is recommended to take multiple sectional lines and average them together to obtain a curve along the beam that represents more data than a single point or single line of data.

2.2 DYNAMIC TEST

2.2.1 DYNAMIC TEST ANALYTICAL WORK

Natural circular frequency associated with various modes of vibration was analytically calculated using the following equation [13]:

$$\omega = (\nu * L)^2 * \sqrt{\frac{E*I}{\rho*A*L^4}} \quad \text{(Eq. 6)}$$

where

v:roots of cos(v*35)*cosh(v*35)+1=0

L: Length of beam, 35 inches.

E: Young's Modulus

I: Area Moment of Inertia

ρ: Density

A: Cross-sectional area

Natural frequency in hertz is calculated from the circular frequency using the following equation:

$$f = \frac{\omega}{2\pi} \quad \text{(Eq. 7)}$$

Young's modulus was determined from an average of experimental frequency data from the accelerometer, strain gauges, and photogrammetry data. Frequency was determined peak to peak. Equation 6 was manipulated to solve for Young's Modulus with the following dimensions,

ρ: Mass Density = 0.000253623

A: Cross sectional area = 3.1563 in^2

L: Beam Length = 35 in

I: Cross section moment of inertia = 0.0657 in^4

f: Average Experimental Frequency = 13.00435

c: (v*L)^2 = 3.5160153

where

$$E = \frac{\rho A L^4}{I}\left(\frac{2\pi f}{c}\right)^2 = \frac{(0.000253623)(3.1563\ in^2)(35\ in)^4}{0.0657\ in^4}\left(\frac{2\pi(13.004)}{3.5160153}\right)^2$$

$$= 9{,}865{,}928\ psi \qquad (Eq\ 8)$$

2.2.2 DYNAMIC TEST COMPUTER SIMULATION

The FEA model developed to analyze the static test condition was also used for the dynamic test condition. The same material properties were maintained. A modal analysis was done to obtain natural frequency modes.

2.2.3 DYNAMIC TEST EXPERIMENTAL WORK

The aim of the dynamic experimental work was to apply a forced vibration to the beam support and to collect data using strain gauges, accelerometers, and the photogrammetry system.

2.2.3.1 DYNAMIC TEST SPECIMEN PREPARATION

Accelerometers manufactured by Endevco [19] were affixed to the beam with removable wax. Accelerometer specifications and calibration information are listed in Table 7.

Table 7 - Accelerometer Specifications and Calibration Information

Manufacture	Model #	Serial #	Range	Calibration Due Date
Endevco	2221E	PB48	2500g	April 2015
Endevco	2221D	12247	2500g	Aug 2013
Endevco	2221D	12251	2500g	Aug 2013
Endevco	2221D	12249	2500g	Aug 2013
Endevco	2220C	RE65	5000g	Aug 2013

Locations of accelerometers are listed in Table 8 and shown in Figure 38. Accelerometers were placed close to the first, second, and fifth mode max locations and second and fifth node locations.

Table 8 - Accelerometer Locations

Location from fixed end (in)	0.00	10.00	17.40	27.10	30.30	35.00
Accelerometer Channel	-	7	8	9	10	11

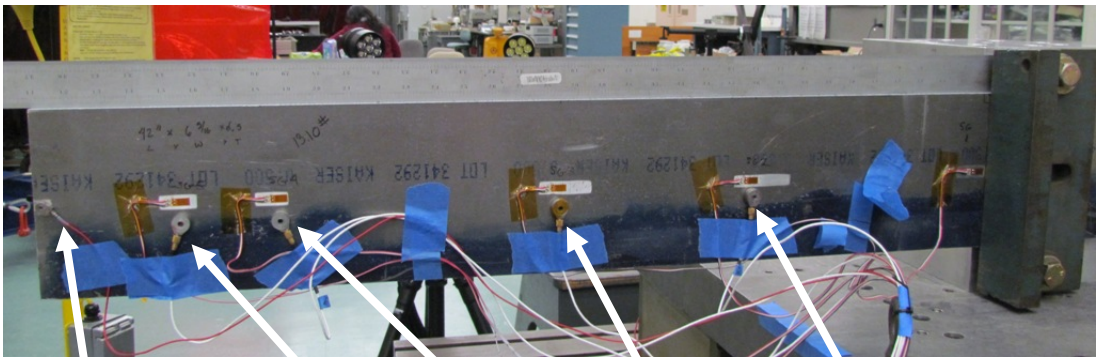

Figure 38 - Accelerometer Locations With Respect to Fixed End

2.2.3.2 DYNAMIC TEST PHOTOGRAMMETRY

The maximum frame capture rate of 96 Hz with camera resolution of 812x1236 pixels was used for this test. Higher frame capture rates are possible up to 367 Hz, however the field of view must be reduced to achieve these higher rates. Since the Nyquist-Shannon sampling theorem requires a sampling rate greater than twice the maximum frequency of the data collected, the 96 Hz sample rate would produce valid data for frequencies up to 46 Hz. The first natural frequency mode of the beam was 13 Hz, however the second mode was 81 Hz. Thus at this camera resolution and sampling frequency, testing was restricted to the first mode of the beam.

The photogrammetry system was triggered with an optical sensor. The sensor was first covered, and then uncovered to initiate the start signal. The optical sensor was also recorded in the strain gauge and accelerometer data collection system at 512 Hz. The photogrammetry, strain gauge, and accelerometer data acquisition system is shown in Figure 39.

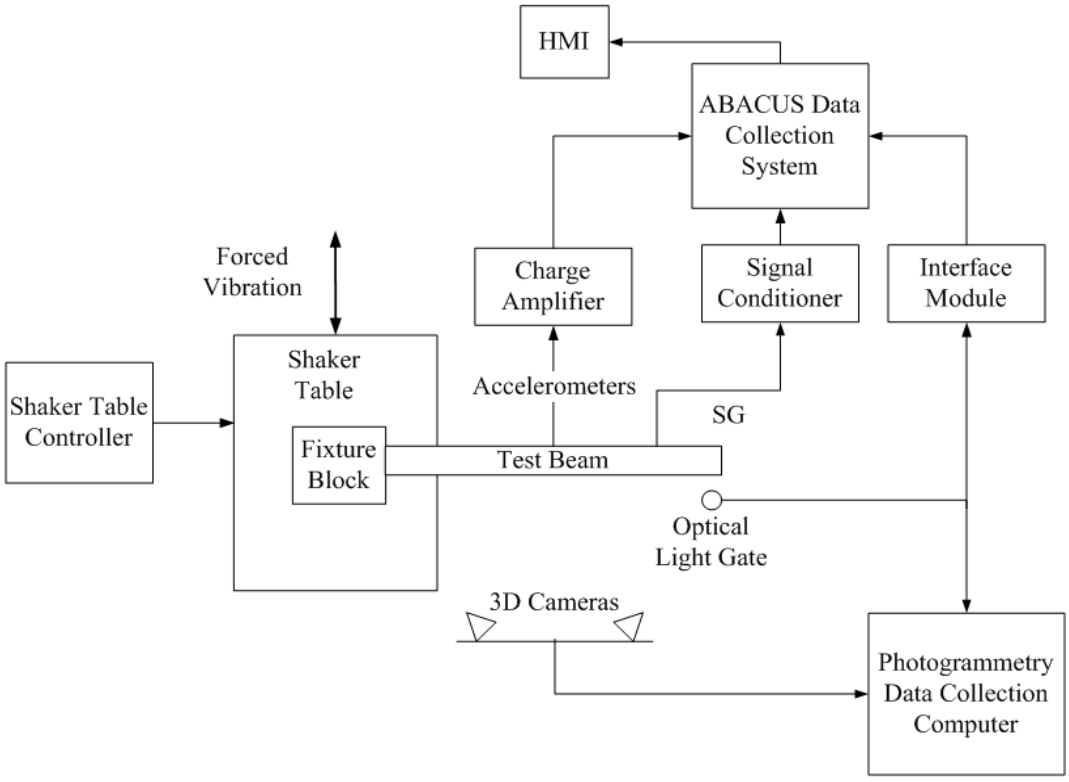

Figure 39 - Photogrammetry Data Acquisition System

2.2.3.3 DYNAMIC TEST SET-UP

The 70 lb aluminum block was mounted on the 137 lb shaker table. The shaker table was set to run at 13 Hz at 1 g-force. The dynamic test set up is shown in Figures 40 and 41. First mode frequency was determined from analytical calculations and confirmed by running a sine sweep and observing the frequencies at which maximum displacement occurred.

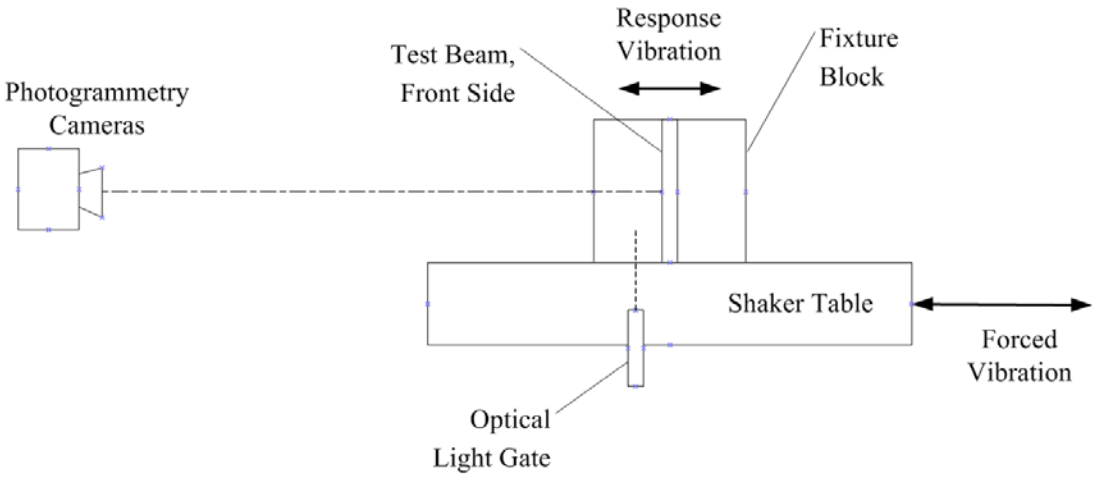

Figure 40 - Dynamic Test Set-up Diagram

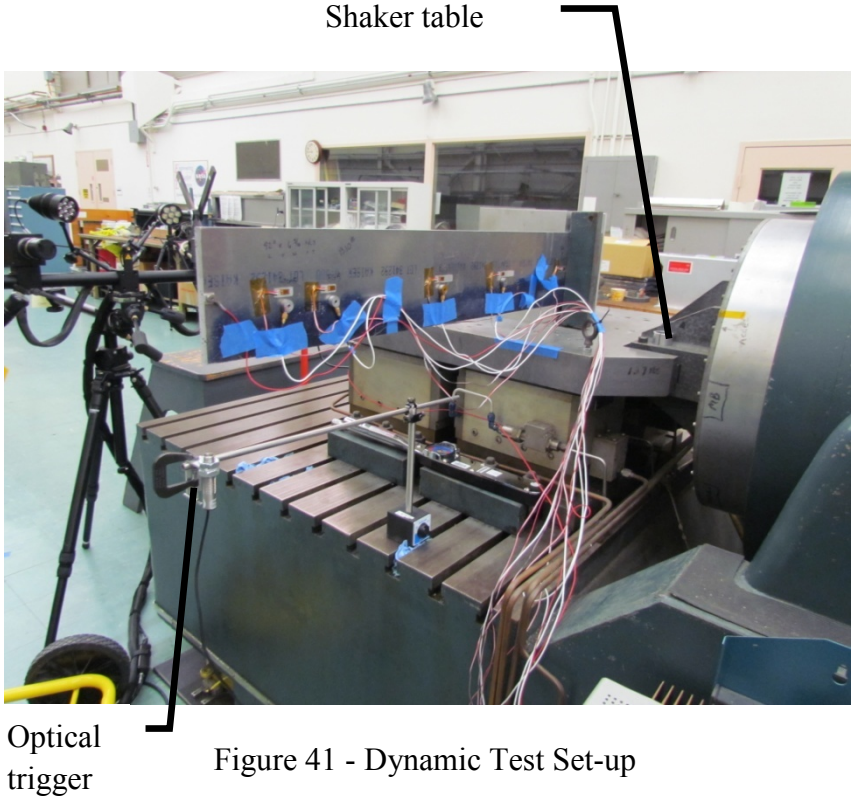

Figure 41 - Dynamic Test Set-up

2.2.4 DYNAMIC TEST RESULTS AND CORRELATION

Dynamic frequency data was collected with accelerometers, strain gauges, and the photogrammetric system. Strain gauge location 2 was selected for strain analysis because it had the highest amplitude and yielded the cleanest data. Other strain gauge locations had an 80 Hz noise that could be filtered out but were not processed for this study. The 80 Hz noise is suspected to be from an attempt to input strain gauge 1 data into the ARAMIS system. Strain gauge 1 data was corrupted in the process. Displacement data for accelerometer 10 was analyzed. Displacement data at the accelerometer 10 location was also analyzed by the photogrammetry system. Photogrammetric displacement data is shown in Figure 42. Photogrammetry strain data was shown in Figure 43. A stage point at the accelerometer 10 position was inserted into all frames of the photogrammetry data for each test analyzed. The resulting displacement vs. time graph and strain vs. time was exported as a text file. The text file was imported into Excel and peak-to-peak frequency was determined. Three test results for strain gauge 2 data are plotted together and shown in Figure 44.

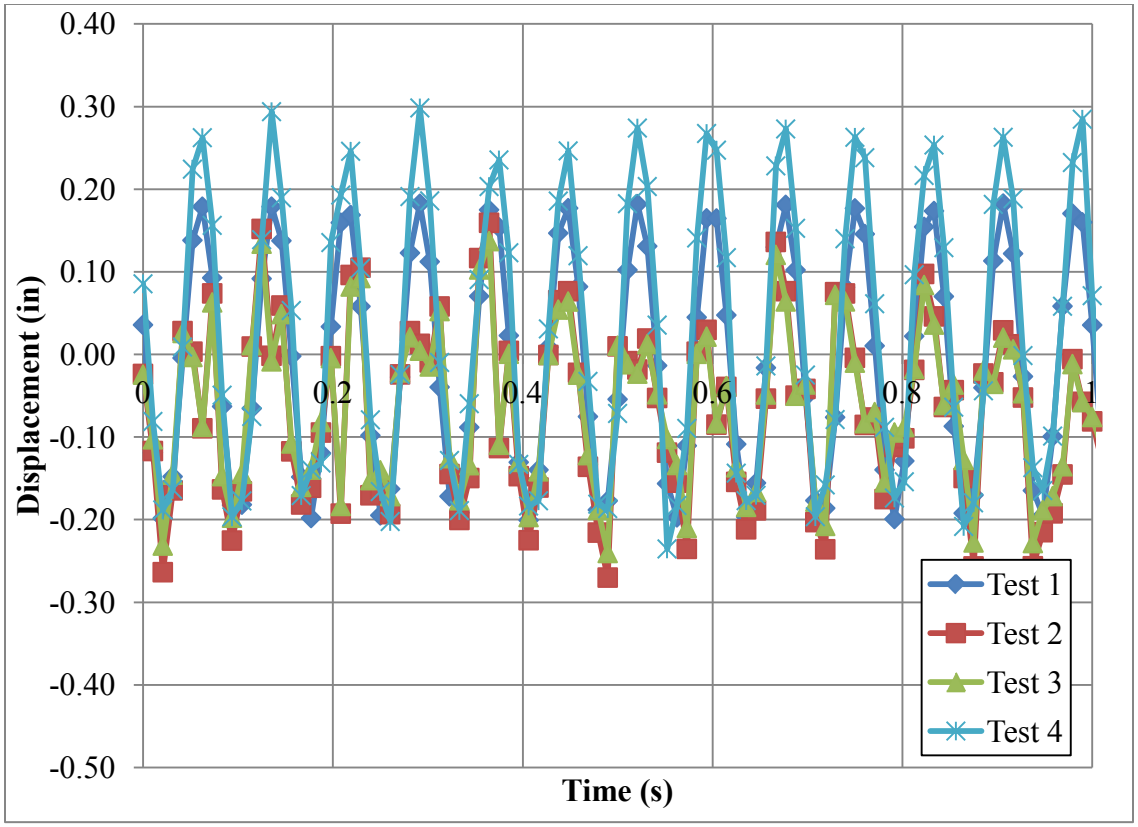

Figure 42 - Photogrammetry Displacement Data at Accelerometer 10 Location

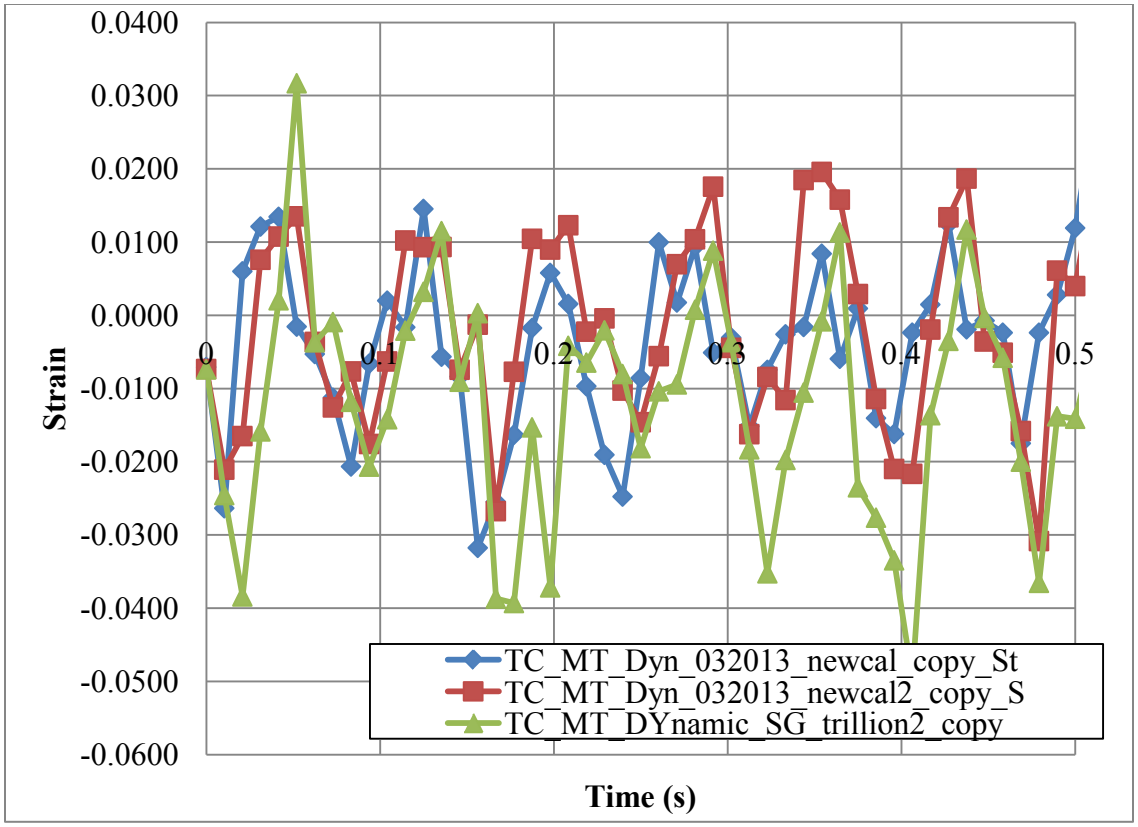

Figure 43 - Photogrammetry Strain Data at SG5 location

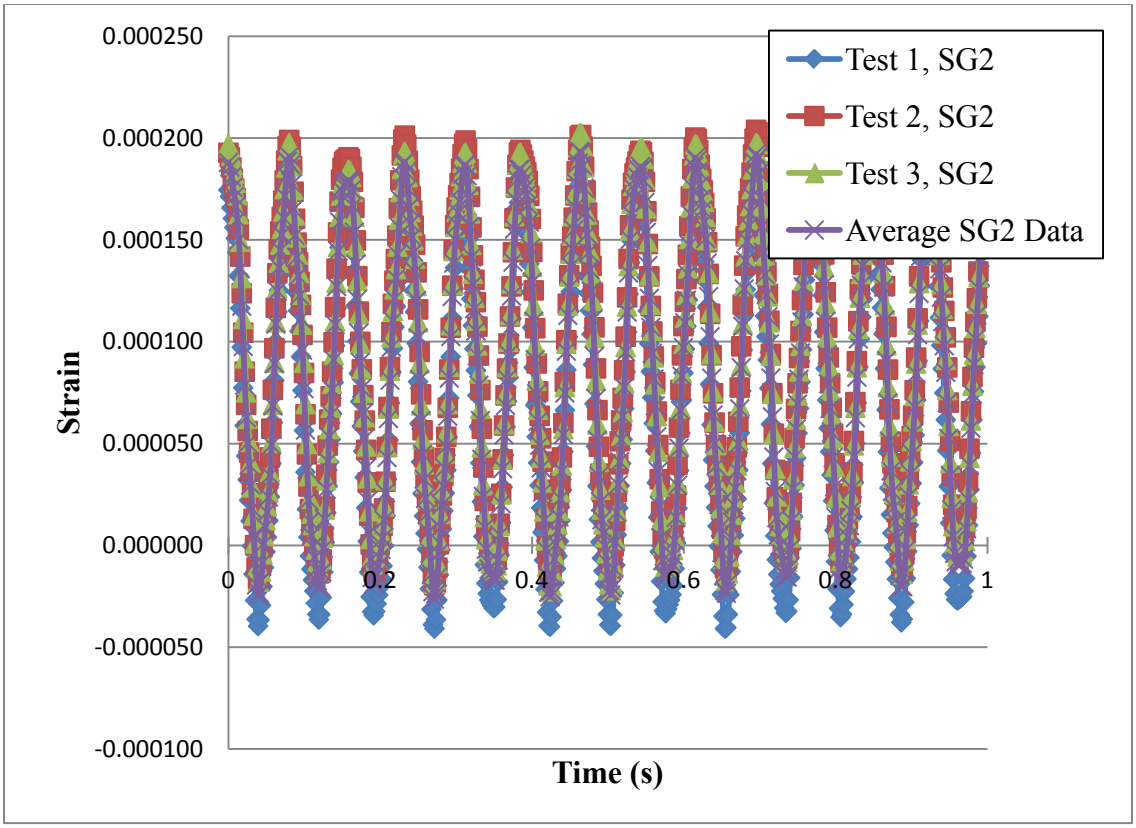

Figure 44 - Strain Gauge 2 Frequency Data

Table 9 - Frequency Results

	Analytical	FEA	Accel10, n=3	SG2 n=3	ARAMIS Displace, Data, n=4	ARAMIS Strain Data, n=3
Frequency, Mode 1	12.91	12.942	12.99	13.00	13.11	13.27
% Deviation from Analytical	-	-0.25	-0.62	-0.73	-1.54	-2.79

The FEA modal analysis was conducted to determine first mode frequency response. Photogrammetry, accelerometer, and strain gauge frequency data was based on three runs and were averaged. Results are presented in Table 8. The percent deviation from the analytical calculations was determined for each case. The FEA had the smallest percent deviation from analytical at -0.25%, followed by accelerometer data at -0.62% deviation. Strain gauge results had a -0.73% deviation. Photogrammetry displacement data yielded a -1.54% deviation while photogrammetry strain data yielded a -2.79% deviation. When the photogrammetry strain and displacement data is averaged together, the frequency is 13.19 Hz with a -2.16% deviation. The percent deviation of photogrammetry is higher than other measures, but is within an acceptable range for a value derived from strain. Photogrammetry frequency based on strain data had a higher percent deviation than displacement. This is increase in deviation is to be expected since strain is derived from displacement information and will not be as accurate.

3.0 CONCLUSION

This study was carried out to build confidence in photogrammetry as an alternative to the application of strain gauges in measuring strain and determining dynamic frequencies of structures. Analytical calculations, computer simulations using finite element analysis (FEA), and experimental work consisting of strain gauges and

photogrammetry were performed. A simple aluminum beam was examined rather than a wind tunnel compressor blade because a simpler geometry allowed for less complex analytical analysis. It was concluded that the method of photogrammetry is a valid and desirable alternative to the traditional application of strain gauges to measure displacement and to determine frequencies. The photogrammetry method showed consistent results for displacement measures with a -0.416% deviation from analytical calculations and 0.399% standard deviation. It must be noted that the low deviation from analytical results for displacement values was non-trivial to obtain. It was necessary to have multiple iterations of the experimental fixture, FEA model and the photogrammetry data had to be reprocessed multiple times.

In areas where strains lower than 0.0001 in/in are anticipated, the ARAMIS system in not an appropriate data collection tool. Strain measures were invalid at lower loads found at the free end of the beam and in the 10 lbs load case. At high loads, photogrammetric strain measures showed a -60.38% deviation from analytical calculations in the worst case (50 lbs, strain gauge 4) and -0.14% deviation for the best case (50 lbs, strain gauge 2). Deviation from analytical calculations at higher strain locations may be due to increased variability of measures from a low signal-to-noise ratio. Better strain correlation can be obtained with higher loads and a higher signal-to-noise ratio. Dynamic frequency data produced an acceptable correlation of -2.79% between analytical calculation and experimental results.

4.0 RECOMMENDATIONS AND FUTURE WORK

The current body of work indicates that photogrammetry is a promising metrology technique. Further investigation of the following items would add to increased confidence in this technique. Multiple section lines corresponding to the area covered by the strain gauges should be examined to determine if averaging more data into the strain measurement would yield static strain measures closer to analytical predictions.

A noise baseline should always be established before data collection to determine the signal-to-noise ratio for the system and a clear understanding of this limitation should be kept in mind during test set-up and when determining for which tests the ARAMIS system could be used.

Further recommendations to expand confidence in this technique would be to use photogrammetry to determine dynamic strain and determine higher mode shapes. The exploration of the strobe synchronization technique is recommended to allow use of slower data collection frame rates while capturing objects moving at a faster speed. More advanced triggering mechanisms and triggering scripts should be investigated.

An advertised capability of the ARAMIS System is to directly compare FEA results to photogrammetry results. An attempt was made to make this comparison however it was discovered that this process is not straight forward. Comparison between FEA and ARAMIS results calls for specific file types [21] that are not created in all FEA programs, and involving conversion of the file by a script that is written in a

non-standard Python code. Further investigation of this feature promises to yield very useful results and should be explored.

5.0 REFERENCES

1 Nguyen, N., (1993) Vibration Control of Compressor Rotor Blades Using Dovetail Damping, *80th Semi-Annual STA Meeting* October 18-19, 1993 Cologne, Germany

2 Nguyen, N., Guist, R., Muzzio, D., (1995) Experimental Investigation of the Rotor Blade Vibration in the Three-Stage Compressor of the 11-by 11-foot Transonic Wind Tunnel, *31st AIAA/ASME/SAE/ASEE Joint Propulsion Conference and Exhibit* July 10-12, 1995 San Diego, CA, AIAA 95-3139

3 Moffitt, F. H. & Mikhail, E. M. (1980). Special Photogrammetric Systems and Applications. In C. Dresser (3rd ed.), *Photogrammetry* (pp.538-584). New York, NY: Harper & Row

4 Moffitt, F. H. (1959). Rectification of Tilted Photographs. In Brinker, R. (2nd ed.), *Photogrammetry* (pp.265-288). Scranton, PA: International Textbook Company

5 Tyson, J., Schmidt, T., & Galanulis, K., (2007) 3D Image Correlation: Measuring Displacement and Surface Strain, *Sensors Magazine*, accessed 9/25/12 http://www.sensorsmag.com/aerospace-military-hs/aerospace/3d-image-correlation-measuring-displacement-and-surface-stra-1383.

6 Schmidt, T., Tyson, J. & Galanulis, K. (2003), Full-Field Dynamic Displacement and Strain Measurement Using Advanced 3D Image Correlation Photogrammetry: Part 1. *Experimental Techniques*, 27(3): 47–50. doi: 10.1111/j.1747-1567.2003.tb00115.x

7 Schmidt, T., Tyson, J. & Galanulis, K. (2003), Full-Field Dynamic Displacement and Strain Measurement Using Advanced 3D Image Correlation Photogrammetry: Part 2. *Experimental Techniques*, 27(4): 22–26. doi: 10.1111/j.1747-1567.2003.tb00118.x

8 Paulsen, U., Erne, O., Moeller, T., Sanaw, G., & Schmidt, T., (2009) Wind Turbine Operational and Emergency Stop Measurements Using Point Tracking Videogrammetry, *SEM 2009 Annual Conference & Exposition on Experimental & Applied Mechanics,* Albuquerque, New Mexico.

9 Tyson, J., Psilopoulos, J., Schwarts, E., &Galanulis, K., (2011) Advanced Material Properties Measurements with Optical Metrology, *SAE International.*

10 Ruther, H., Smit, J., Kamamba, D. (2012) A Comparison of Close-Range Photogrammetry to Terrestrial Laser Scanning for Heritage Documentation, *South African Journal of Geomatics*, Vol. 1. No.2, 149-162

11 Standard Test Method for Determining the Volume of Bulk Materials Using Contours or Cross Sections Created by Directed by Direct Operator Compilation Using Photogrammetric Procedures, *ASTM* D6172-98 (2010)

12 Littell, J. Schmidt, T., Tyson, J., Oliver, S., Melis, M., Ruggeri, C. and Revilock, D., Photogrammetry Measurements During a Tanking Test on the Space Shuttle External Tank, ET-137, *SEM XII International Congress and Exposition on Experimental and Applied Mechanics;* 11-14 Jun. 2012; Costa Mesa, CA; United States Doc 20120011261

13 Takács, G. &Rohaľ-Ilkiv, B. (2012). Basics of Vibration Dynamics. *Model Predictive Vibration Control Efficient Constrained MPC Vibration Control for Lightly Damped Mechanical Structures* (pp.40-46) Springer

14 Esbach, O., (1952) Beams of Uniform Cross section, (2nd ed.), *Handbook of Engineering Fundamentals*, (pp.29-39). New York, NY. John Wiley & Sons Inc.

15 "PATRAN Product page," accessed June 9, 2013,http://www.mscsoftware.com/product/patran.

16 "NASTRAN Product page," accessed June 9, 2013, https://www.mscsoftware.com/product/msc-nastran.

17 "Vishay Precision Group Company Page, " accessed June 9, 2013, http://www.vishaypg.com/micro-measurements/

18 "Strain Gage Application Instruction Bulletin B-237," accessed June 9, 2013, http://www.vishaypg.com/docs/11137/b-137-4-.pdf

19 "Endevco Company Page, " accessed June 9, 2013, https://www.endevco.com/

20 "ARAMIS System Product Page," accessed November 11, 2012 , http://www.gom.com/metrology-systems/system-overview/aramis.html,

21 ARAMIS User Manual – Software v6.3 and Higher aramis-v6-3_1st_en_rev-a (2011), ARAMIS, GOM mBH, Braunschweig Germany

APPENDIX A: CALIBRATION INFORMATION

	Manufacturer	Model	S/N	calibration	Range	Accuracy	Slope
Load Cell	Interface	SM-250	B61455	6/13/2012	0-250 lbs	+/- .03% FS	77849.39 lbs/(V/V)
LVDT	Bcurns inc. 2.5" 5000Ω Align-c-pot trans.	80294-20015 63016	258230 (M114912)	11/27/2002	0-2.5"	+/- 0.0031"	2.5903 1827 inch/(V/V)
LVDT Signal Conditioner			1460	3/20/2012			
LVDT Signal Conditioner			1456	3/20/2012			